REVIEW ARTICLE

Shock wave interactions within concave cavities

David MacLucas[1,2] · Beric Skews[1] · Harald Kleine[3]

Abstract

The interaction of a plane shock wave in air with concave profiles has been used in the past mainly to understand the nature of shock wave focusing. The current study examines the complex two-dimensional flow field resulting from the interaction of a plane shock wave entering a symmetrical cavity with curved walls. Of particular interest are the development of reflection patterns of the incident shock wave at the profile wall and the process of gas dynamic focus. These principal flow features are examined across a wide range of different reflector shapes. This includes a review of previously studied profiles such as cylindrical and parabolic, and also of a number of additional profiles, including compound profiles, where an inlet profile merging with that of the main cavity is shown to have major effects on the focusing mechanism and pressures. The various reflector shapes were specified by varying the shape of the profile and the depth-to-aperture ratio. The strength of the incident plane shock wave was limited between Mach numbers of 1.04 and 1.45. The principal flow features were established and examined experimentally using a variety of qualitative and quantitative flow visualization techniques, supplemented with numerical results. Time-resolved high-speed imaging was used to capture the interaction providing the unique ability to track the various transient flow features over the course of the interaction. The three primary factors that influence the maximum pressure amplification at focus, and the focus mechanism, are the incident shock strength, the depth-to-aperture ratio of the profile and an inlet profile leading into the main cavity, if present. An inlet profile results in higher-pressure amplifications for corresponding shock strengths and depth-to-aperture ratios. Increases in the depth-to-aperture ratio increase the maximum pressure amplification observed at focus. This occurs due to a combination of factors including: the strengthening of the individual shock waves involved in focus; the duration of focus; and the strengthening of a compressive flow field that develops adjacent to the shock system during focus. The compressive flow field adjacent to the shock system at focus is shown to be of great importance to the focus process.

✉ Beric Skews
  beric.skews@wits.ac.za

  David MacLucas
  DMaclucas@csir.co.za

  Harald Kleine
  h.kleine@adfa.edu.au

1 Flow Research Unit, School of Mechanical, Industrial and Aeronautical Engineering, University of the Witwatersrand, PO WITS, Johannesburg 2050, South Africa

2 Defence and Security, CSIR, PO Box 395, Pretoria 0001, South Africa

3 School of Engineering and Information Technology, ADFA, University of New South Wales, PO Box 7916, Canberra, BC 2610, Australia

Graphic abstract
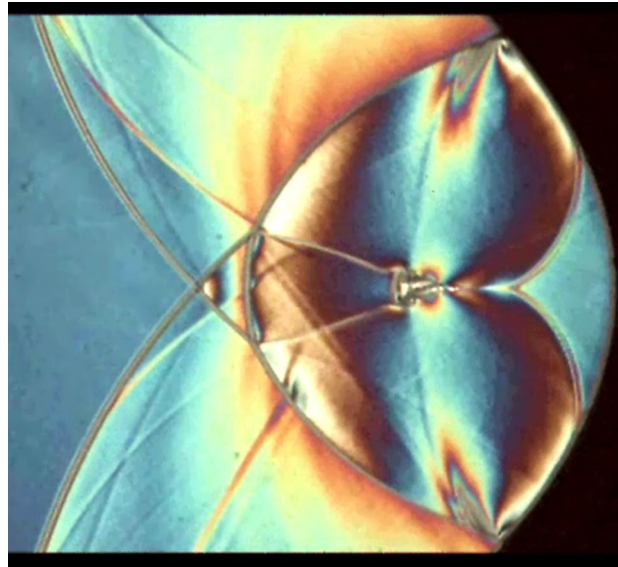
1 Introduction

The earliest study relating to shock wave focusing was by Guderley (1941) followed ten years later by Perry and Kantrowitz (1951) who produced the first schlieren images of the focusing process. One of the first experimental verifications of Guderley's solution was given by Dennen and Wilson (1962) using an exploding thin metallic film on the inner surface of a glass cylinder. Knystautas et al. (1969) were one of the first to obtain schlieren images of the focusing shock. An early review of the field was given by Grönig (1986). This identified the increasing areas of science and engineering where the production of regions of high pressure is of interest and has led to a variety of different studies. These range from initiation of detonations to underwater focusing studies relating to fracturing of kidney stones. An interesting case is the initiation of a shock wave using a spark discharge at one focal point of an elliptical cavity resulting in a focused shock wave at the other focal point (Gustafsson 1987). A very nice theoretical analysis based on Whitham's theory of geometrical shock dynamics (GSD) of the experimental work of Sturtevant and Kulkarny is given in Cates and Sturtevant (1987). The attainment of extremely high focal pressures has been demonstrated for a converging cylindrical shock wave (Apazidis et al. 2012) with a more comprehensive coverage given in a recent book (Apazidis and Eliasson 2019).

The interaction of a plane shock wave with a concave reflector profile has been used primarily for examining and understanding shock wave focusing and, in particular, the pressure amplification which occurs at focus. The emphasis on understanding the mechanisms governing the focal pressures and predicting the magnitude thereof, is useful in numerous applications. These include the design of future supersonic aircraft where minimizing the focal pressures that occur during sonic boom focusing is important (Marchiano et al. 2003) and in the medical procedure of extracorporeal shock wave lithotripsy (Sturtevant 1989). The interaction has also found use in examining fundamental curved shock wave reflection phenomena and the development of curved shock wave reflections (Skews and Kleine 2009) along with development of Kelvin–Helmholtz instabilities in shear layers (Skews and Kleine 2007; Shadloo et al. 2014). This highly complex transient flow field has also been studied using numerical simulation (Liang et al. 1999; Kim et al. 2003) and in the validation of high-order numerical schemes (Taieb et al. 2010).

1.1 Background

Of particular interest in the context of the current paper is the focusing of an initially plane shock wave propagating into a cavity. The case of a cavity with symmetrically placed plane walls has been given by Bond et al. (2009) and in a log-spiral duct by Inoue et al. (1995) For symmetrical cavities with curved walls, the relevant background is the work of Sturtevant and Kulkarny (1976), Nishida (1989) and Izumi et al. (1994). The work of Babinsky et al. (1998)

is of particular significance. These contributions will be expanded on later. A book by Takayama (2019) containing a large compilation of images has very recently become available. These represent the results of forty years of study using holographic interferometry, and some of the reproduced images cover a wide range of cavity shapes.

This paper summarizes the results of numerous shock focusing studies by presenting a generalized description of the gas dynamic processes during the interaction of a shock wave with a concave reflector. Specific characteristics depending on the geometry of the reflector are highlighted, and on the basis of this background, new results are presented that indicate where the existing knowledge may not yet be sufficient. Particular emphasis is put on compound profiles and the addition of inlets to the reflector.

The interaction of a plane shock wave with a concave profile can result in a number of different reflection patterns. The reflection pattern is mainly influenced by the shape and initial slope of the concave reflector profile and, to a lesser extent, by the strength of the plane incident shock wave. For profiles with no initial slope, no initial reflection of the incident shock wave occurs as is typical for cylindrical profiles with tangential entry, as sketched in Fig. 1, with corresponding images in Skews and Kleine (2009). A series of successive compressive acoustic signals, C, develops as a result of the increasing slope of the profile wall which the incident shock wave experiences. These compressive waves converge with time forming a kink in the incident shock wave, which develops into a Mach reflection, consisting of the incident wave I, reflected wave R, a Mach stem M and a shear layer L. As identified in Ben-Dor (2007), the Mach stem, M, will grow for a short duration, but as the slope of the profile wall steepens the reflection becomes inverse.
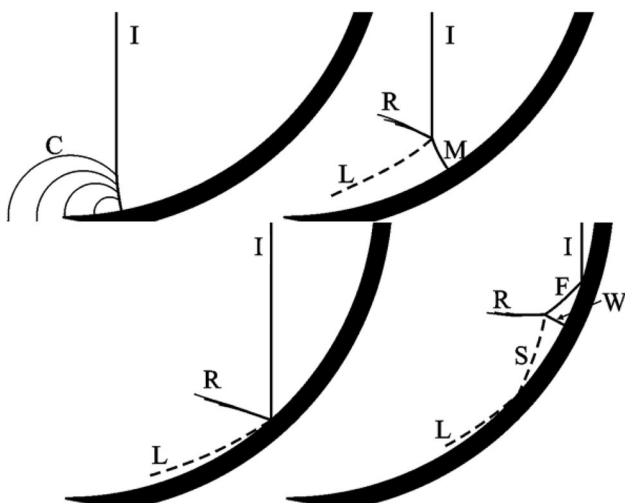
The Mach stem will then decrease in length until the reflection temporarily apparently becomes regular as observed by Babinsky et al. (1998), and in a later work by Gruber and Skews (2013) for weak shocks, although interpretation may well depend on image resolution being unable to distinguish a very small Mach stem. The reflection will then progress to a special form of regular reflection termed a transitioned regular reflection (TRR). The TRR consists of a regular reflection consisting of waves I and F, followed by a Mach reflection as indicated in the last sketch in Fig. 1. This transition from an inverse Mach reflection to a TRR was initially observed experimentally in cylindrical profiles in Ben-Dor and Takayama (1986) and subsequently by others. However, the transition from a regular reflection to a TRR-like structure without a preceding Mach reflection has been observed in a shallow parabolic profile by Izumi et al. (1994) and is also found in the compound profile used in this work. A wall shock, W, arises to balance the pressures encountered in the rapid transition between the regular reflection and the TRR (Ben-Dor 2007).

Cylindrical profiles may be designed to have no initial slope, but if a cylindrical profile is truncated, as for some cases given in Takayama (2019), or if the profile has a different shape (e.g. parabolic or elliptic), the initial slope is usually finite. In such a case, the initial interaction of the shock with the reflector is an irregular reflection if the initial slope is below the transition angle or a regular reflection for large initial slopes above the transition angle. For profiles with an initial small finite slope such as to generate a Mach reflection, as in the parabolic cavity illustrated in the first frame in Fig. 2, the pattern consists of the incident shock, I, and reflected shock, R, connected to the surface with the
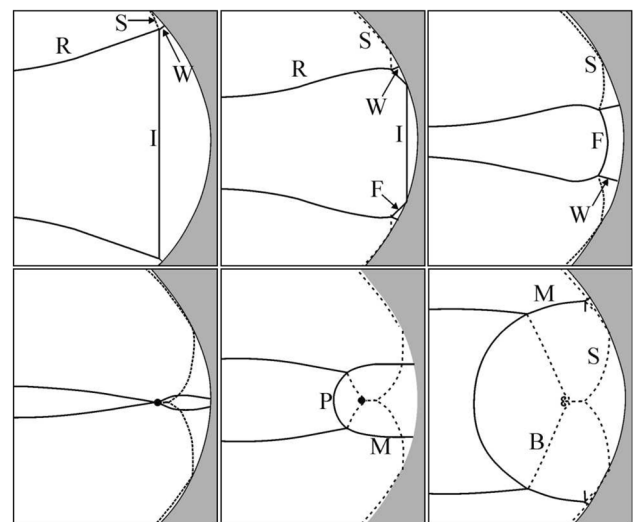

Fig. 1 Schematic of the main features of shock wave entry into a cylindrical profile with no initial slope

Fig. 2 Schematic of the main features in a medium-strength shock wave interaction at the base of a parabolic cavity

Mach stem W, also referred to as the wall shock. A shear layer, S, is shed from their confluence.

As the shock wave system progresses into the profile, the shock wave, F, is reflected from the base of the profile, as indicated in the third frame. The curved nature of this wave arises due to the continually changing slope of the base of the profile, from which the incident shock wave I is reflected. Once the incident shock wave is fully reflected from the base of the profile, a three-shock reflection remains where the three-shock intersection of the reflection is moving towards the profile centre line. The start of gas dynamic focus has been defined by Sturtevant and Kulkarny (1976) as the point where the three-shock intersections of the two three-shock reflections meet on the centre line of the profile as indicated in the fourth frame in Fig. 2. Thereafter, a new Mach reflection forms and also a set of three-shock reflections consisting of: the reflected shock wave, R, the common stem, P, the main reflected wave, M, and new shear layers, B. The main reflected wave forms from the combination of the two wall shocks, W, see Skews and Kleine (2007).

The shape of the entrance to the cavity has an influence on the subsequent flow as shown in Fig. 3. For cavities with a sharp leading edge, the profile tip will generate an acoustic wave which is the leading wave of the following compression and sometimes referred to as a tip signal, TS, or a corner signal C. For the case of a small finite entry angle, the wave is a reflected shock, such as the Mach stem in a Mach reflection, changing to an acoustic wave below the test piece. For a steeper inlet angle, a regular reflection can result. Where the reflected wave arises from the entrance lip of the cavity, it is sometimes referred to as a lip shock. If the reflection point moves supersonically with respect to the flow behind it, the corner signal cannot catch up with the point of reflection as shown in the right-hand sketch.

The first comprehensive study of shock wave focusing in a cavity is that of Sturtevant and Kulkarny (1976). Three parabolic cavities of the same aperture, but differing in depth, were tested. Their depth-to-aperture ratios are 0.053, 0.105 and 0.21, respectively. Tests were conducted over a range of Mach numbers from 1.005 to 1.5. It was shown that
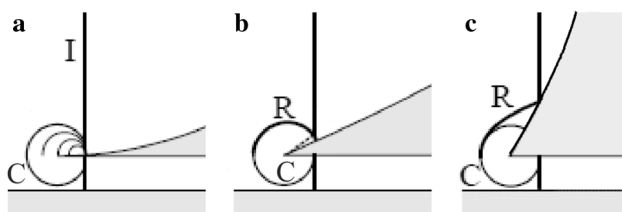
a nonlinear flow field develops near focus and this limits the pressure amplitude at focus. Three waves were identified that participate in the focus process: the reflected incident shock wave, F, that converges as it nears focus; compressive diffracted shock fronts , R; and what Sturtevant and Kulkarny termed a set of diffracted expansion waves arising from the corners of the reflectors. Due to window size limitations of the experimental configuration compared to cavity diameter, Sturtevant and Kulkarny did not recognize that what they termed a set of diffracted expansion waves is actually a result of an earlier reflection. Skews and Kleine (2007) showed that these waves are the Mach stems of a TRR.

Nishida (1989) examined shock focusing of a plane incident shock wave in two parabolic profiles using experiment and simulation. Different depth-to-aperture ratios were used. It was found that peak pressure amplification increases with increasing Mach number below Mach 2.0. In addition, peak pressure amplification is enhanced if the depth-to-aperture ratio is increased, and the point of gas dynamic focus moves closer to the base of the profile with increasing Mach number. Another computational/experimental study by Izumi et al. (1994) relied on parabolic profiles with larger depth-to-aperture ratios. The results from the deepest profile, with a depth-to-aperture ratio of 0.5, illustrated that the reflected shocks cross prior to focus and remain crossed thereafter. Unfortunately, the shape of the focal region was not examined, but the start of focus remains the same: the triple points of the Mach reflections from the top and bottom of the profile meet on the centre line of the profile. The authors also classified the focus process according to the shape of the reflected shocks, R, before, at and beyond focus.

One of the most creative shock focusing studies to date is by Babinsky et al. (1998). It is an examination of the effect of the inlet shape of circular reflectors on shock focusing. Three profiles with circular inlets with radii double, equal to and half the radius of the circular reflector were tested along with a circular profile without an inlet; the reflector without an inlet was used to establish the standard focus mechanism for comparison. Interferograms used for this study are given in Takayama (2019). Unlike previous studies (Izumi et al. 1994; Nishida 1989; Sturtevant and Kulkarny 1976) which did not consider the incident shock wave reflection behaviour prior to focus, such as described earlier, the process of going from a Mach reflection to a transitioned regular reflection was included in both the numerical and experimental studies. It was found that the effect of a curved inlet is substantial, with peak pressures being nearly 50% higher than in the simple circular cavity, with maximum pressure increasing with increases in the radius of the circular inlet. The pressure is shown to increase in multiple jumps to the peak focal pressure differing from the standard reflector where focus is characterized by a single jump to the peak pressure. The increase is ascribed as a result of a change in

Fig. 3 Initial reflection of the plane shock wave I and development of the tip signal TS or the corner signal C as observed in **a** smooth entry cylindrical profile, **b** shallow finite-angle concave profile and **c** steep concave profile with the corner signal following the reflection point

the standard focus mechanism described above. The authors attribute the increase in peak pressure to the strengthening of both the reflected shock of the incoming Mach reflection and the Mach stem of the TRR. Increases are also a result of the timing of the arrival of the various shock waves in the focal region. Unfortunately, they did not provide any flow visualization images of the focal region showing the new focus mechanism. Nonetheless, this work shows that inlets can play a substantial role in the focusing process, and therefore, they are used in the current study as well.

In understanding the mechanisms of the development of shock patterns when reflecting off curved surfaces, the use of a novel perturbation technique, Skews and Kleine (2009), for studying transient two-dimensional flows, has provided valuable insight into the formation of curved shock wave reflections and shock wave focusing. Weak perturbations, generated by the passing of a shock over transverse perturbation sources placed at specific points on the wall of a test piece, can be used as a diagnostic tool in unsteady flows. These sources generate very weak waves, where the points along the wave will convect according to a combination of the local sound speed and the local flow velocity they encounter. Not only are they a valuable visual aid, but underline an important concept in gas dynamics regarding how changes in boundary conditions are communicated to

the subsequent flow and the limit of their influence on the ensuing flow.

The top row of images in Fig. 4, using the perturbation technique, shows the evolution of flow in the initial part of a cylindrical cavity. In the first frame, the compressive wavelets coming off the surface cause the incident shock to curve forward near the surface. In the second frame, some of these waves meet resulting in a reflected shock of finite strength together with the associated shear layer. It is interesting to note that the wavelets from the entry part of the surface do not contribute to the shock wave development, but, because they are compressive, will result in a very slight strengthening of the incident wave, although this is imperceptible. The Mach reflection then grows in size and becomes a stationary Mach reflection and then inverse Mach reflection, with the triple point moving towards the surface. In the fourth frame, the triple point has reached the wall and the shear layer is abandoned. Furthermore, the early perturbation signals which had been contacting the incident shock wave are now left behind.

The subsequent evolution showing pre- and post-focus conditions is given in the bottom row of the figure. In the first frame, the reflection develops into a transitioned regular reflection with the development of the wall shock and shear layer which are carried through after the incident

Fig. 4 Shadow images of the features in a medium-strength shock wave interaction in a cylindrical cavity, using perturbations. Top four images for a Mach 1.22 shock reflecting off a 130-mm-radius surface. Images at 40 μs interval. Bottom row for a Mach 1.32 wave in a 64-mm-radius cavity. Images at 28 μs between frames
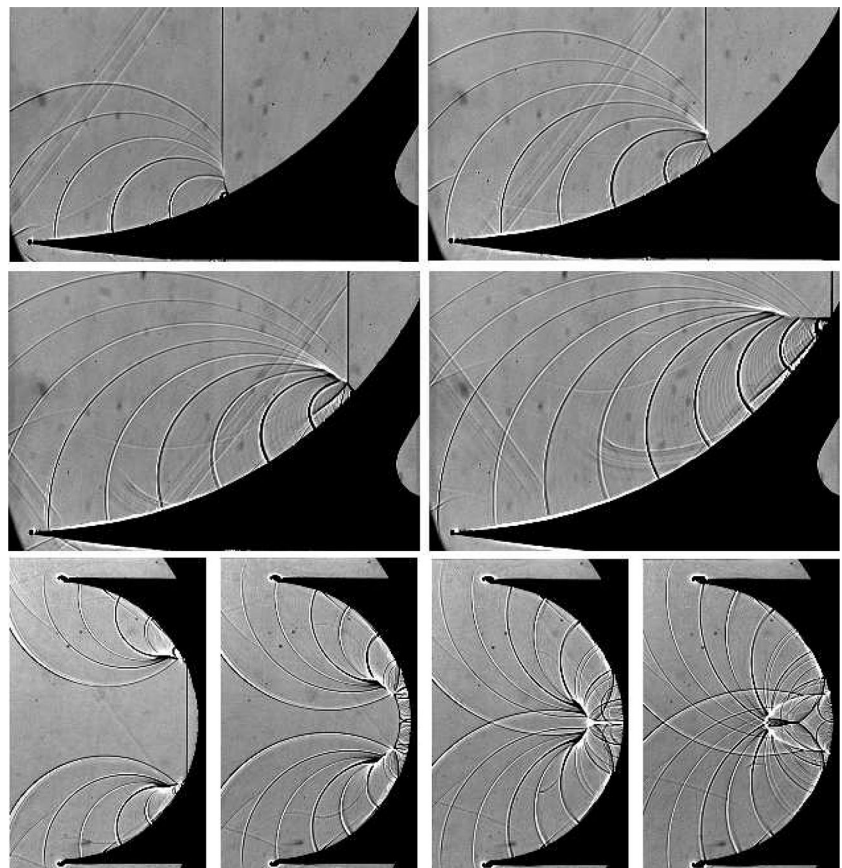
wave reflects off the base of the cavity as shown in the second frame. Gas dynamic focus is shown in the third frame where the shear layers meet on the symmetry plane, as has been defined in the literature. The main reflected wave then develops with the shear layers combining, forming into a jet and then separating, leading to later development of vortices. The complex patterns developed at a later stage with the merging of the shear layers and the development of a mushroom-shaped pair of vortices, as well as marked development of Kelvin–Helmholtz instabilities on the shear layer, are fully treated in Skews and Kleine (2007).

The manner in which the compressive information arising off the wall propagates into the cavity for a cylindrical and parabolic cavity is shown in Fig. 5, using the perturbation technique. The cavity profile shape has a significant influence on the development of focus. For the cylindrical case, the first frame shows how the wavelets from each side coalesce to form the reflected shock of the Mach reflection. The earliest wave from the model tip does not contribute to this. For the corresponding early case for the parabolic surface, all compression wavelets contribute to forming the shape of

the reflected wave which started from the model inlet. The centre images show the condition near focus where many, but not all, of the perturbations converge. The final images show the formation of the main reflected wave coming out from the cavity. Perturbations from both top and bottom contribute to the reflected wave strength except in the parabolic surface where some are still contributing to the reflected wave from the cavity entrance. The dotted yellow lines show where the compression waves off the wall converge and contribute to the shock waves.

A very effective visualization technique for interpreting such flows is the use of shearing interferometry Kleine (2001), Oertel and Oertel (1989). In this method, two light rays passing through the flow at close proximity are made to interfere with the resulting interference pattern showing contours of constant density gradients. An example is given in Fig. 6. The colour fringes are related to the density gradient in a preset direction through the calibration of the flow visualization system. The inset in the first frame shows the fringes generated when passing through a long focal length lens, thereby enabling calibration and facilitating

Fig. 5 Shadowgraph images illustrating the limit of perturbations. Top: cylindrical reflector. Bottom: parabolic reflector. The incident shock wave has a Mach number of 1.23, and the depth-to-aperture ratio in both cavities is 0.5. Instant of shown flow field (in μs) is indicated on the bottom right corner of each frame
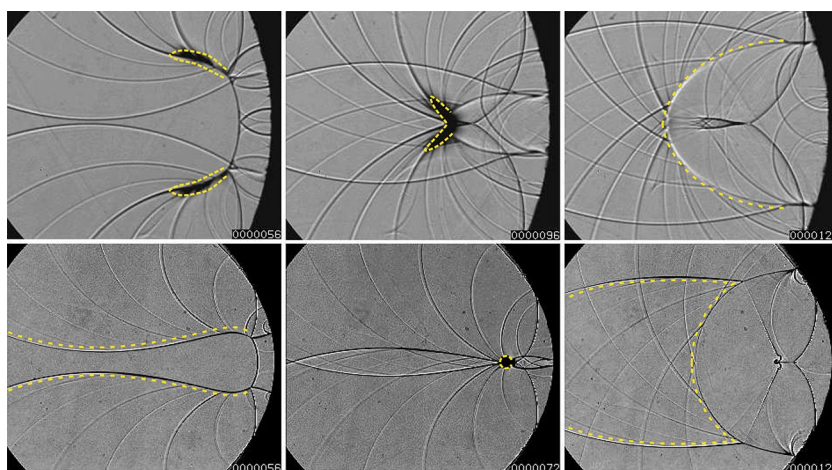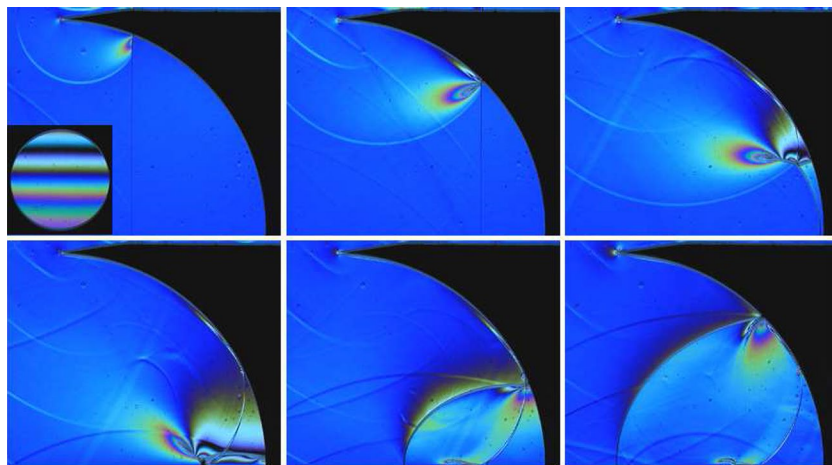

Fig. 6 Shearing interferometry visualization of a Mach 1.23 plane shock entering a cylindrical cavity of depth-to-aperture ratio 0.5. Images are 50 μs apart

interpretation of the flow. The images shown were taken in infinite fringe mode with the background (i.e. no flow) fringe set on the blue fringe, corresponding to the central fringe in the calibration image. Thus, in the first image when the incident shock curves forward the increasing density behind the shock due to its increasing strength is very evident, with the density gradients passing from the blue fringe through light blue, yellow, red and further down through the colours in the calibration image. The second frame shows Mach reflection and the third frame transitioned regular reflection. The first frame in the bottom row is just very shortly after focus where the shear layers from either side meet. The final two frames show the development of the main reflected wave from the cavity with the change in colour just ahead of it indicating the weakening as it propagates outwards. One of the limitations of this technique is that the interference fringes result from two polarized beams, which are separated by a small distance, so no features smaller than this distance can be resolved. This fact is evident in the slight grey area surrounding the upper edge of the curved surface, as well as in affecting the corresponding thickness of the shock waves. The shear introduced by the separation of the polarized beams essentially creates a double image of all discontinuities in the direction of the separation (Kleine 2001).

2 Experiments

Experiments consisted of two test sets. The first set was performed with the aim of gathering pressure history data from various locations in the flow field of a parabolic profile model in order to validate the numerical scheme. These tests were conducted in a double-diaphragm compression chamber shock tube with a rectangular cross-sectional test section 180 mm high by 76 mm wide. The shock tube is specifically suited to taking pressure measurements owing to the expansion chamber being constructed from coarse flake grey cast iron shown to have good vibration damping properties. Some schlieren and shadowgraph tests were also done in this tube.

The main facility used for the majority of tests was a conventional diaphragm-operated shock tube with a rectangular cross-sectional test section measuring 150 mm high by 75 mm wide. This was chosen due to the availability of a well-established set of flow visualization set-ups as well as different high-speed cameras. The optical system was arranged in the standard Z-type configuration using two schlieren mirrors of equal focal lengths (2624 mm focal length; 240 mm dia.). A cylindrical lens was included in the set-up to minimize the astigmatic difference between foci in the sagittal and meridional planes. Shadowgraphy, schlieren imaging and shearing interferometry were implemented. For monochrome visualizations, a Shimadzu HPV-1

high-speed camera with 312 x 260 pixels resolution was used. Polychrome visualizations were conducted with a prototype developed by NHK, which has a resolution of 720 x 410 pixels, or a Phantom 710 (resolution 320 x 160 pixels at the selected frame rate). The former two cameras can be operated up to one million frames per second (fps) without changing the resolution, and the last one is typically operated at frame rates below 100,000 fps as the resolution has to be decreased for increasing frame rates. The shearing interferometry system utilized a Wollaston prism (separation angle ϵ of 1 arc minute) as the shearing element, resulting in a shear distance of 0.764 mm ($d = f_2\epsilon$). The system was operated in infinite fringe mode where the sky blue fringe was selected as the background and reference fringe. Calibration of the system followed the procedure outlined in Kleine (2001), where a calibration lens of large focal length (10.27 m) is imaged in the test section. The fringes in the calibration image are equivalent to a colour-coded phase shift where the phase shifts, associated with each colour fringe, are tabulated in handbooks (Oertel and Oertel 1989). The current system calibration covers a range of $-84\,\mathrm{kgm^{-4}} \leq \partial\rho/\partial x \leq 74\,\mathrm{kgm^{-4}}$. The measurement direction of the system was set to resolve density gradients in either the horizontal or the vertical direction (i.e. either vertical or horizontal fringes) depending on which component of the flow field was to be visualized. The direction for increasing or decreasing density gradient magnitude, $\partial\rho/\partial x$ or $\partial\rho/\partial y$, for a fringe of interest, is established by comparing the fringes on either side of the selected fringe. Note that any flow field phenomena smaller than the shear distance of the system cannot be resolved. As mentioned above, the system will produce double images approximately 5 pixels wide in the direction of shear, due to the presence of discontinuities (body contours, shocks and contact surfaces) in the field of view. Interpretation of any flow features adjacent to such discontinuities should be done with care. In both shock tubes, the shock Mach number is determined via a number of time-of-flight measurements with pressure transducers mounted flush in the shock tube/test section walls. The associated measurement uncertainty for the shock Mach number is at most ±0.01 for all tests reported here.

3 Numerical simulation and validation

3.1 Numerical scheme

The numerical solver uses the compressible Euler equations which are solved using a finite volume vertex-centred scheme. For this type of study, it is shown in Taieb et al. (2010) that an Euler-based approach is sufficient for adequately resolving the flow field even for weak Kelvin–Helmholtz instabilities which develop on the shear layers. The

solution is stabilized by adding dissipation implicitly in the evaluation of the Euler fluxes which are computed using a flux vector splitting method, as per the AUSM+ scheme (Liou 1996). Time integration is explicit, where a four-stage Runge–Kutta scheme is used ensuring second-order temporal accuracy. The flow solver has second-order spatial accuracy, where a linear variation of the solution within a cell is reconstructed. The reconstruction procedure works in combination with a multidimensional limiter (Barth and Jesperson 1989) to limit overshoots and oscillations in the reconstructed solution. Dynamic unstructured triangular meshes are used whereby the maximum density gradient error within a cell is maintained within a user-defined value (1%) of the maximum allowable density gradient error found across the entire mesh.

Wall boundary conditions were used for the profile and symmetry plane, while a supersonic inflow/outflow condition was specified for the outlet. Prior to comparison between numerical and experimental results, mesh independence was established by determining the limits of cell size for which the pressure history curves remained converged. The peak pressures at focus itself, across the Mach number range, were found to be mesh-dependent, as also found in Izumi et al. (1994), but the solution of the subsequent flow post-focus remained mesh-independent. Validation of the numerical scheme was performed by comparing numerical and experimental pressure histories at a number of locations within the flow field for various Mach numbers. For comparison purposes with the experimental data, the numerical pressure histories were averaged over the same area as the pressure transducer face to provide a more representative solution.

3.2 Validation tests

Shock focusing tests were conducted on a parabolic profile cavity, $x = -10y^2$, with an aperture of 160 mm and depth-to-aperture ratio of 0.4. Pressure traces, using PCB transducers, were obtained from various sites in the cavity field. In the pressure tests, the fast-response pressure transducers (uncertainty ±1.3%) were mounted flush in the shock tube side wall and recorded the static pressure generated by the passing shock wave and its reflection(s). The transducers were spaced in a way that they yielded approximate point measurements of the static pressure without any form of mutual interference. Figure 7 shows comparisons between numerical and experimental traces for two locations in the flow field at two Mach numbers. These show excellent agreement between the numerical and experimental results. The inset shows the position and relative size of the transducer together with an indication of the flow field at a particular time. The passing of other features over the transducer is identified and can be correlated with the wave evolution
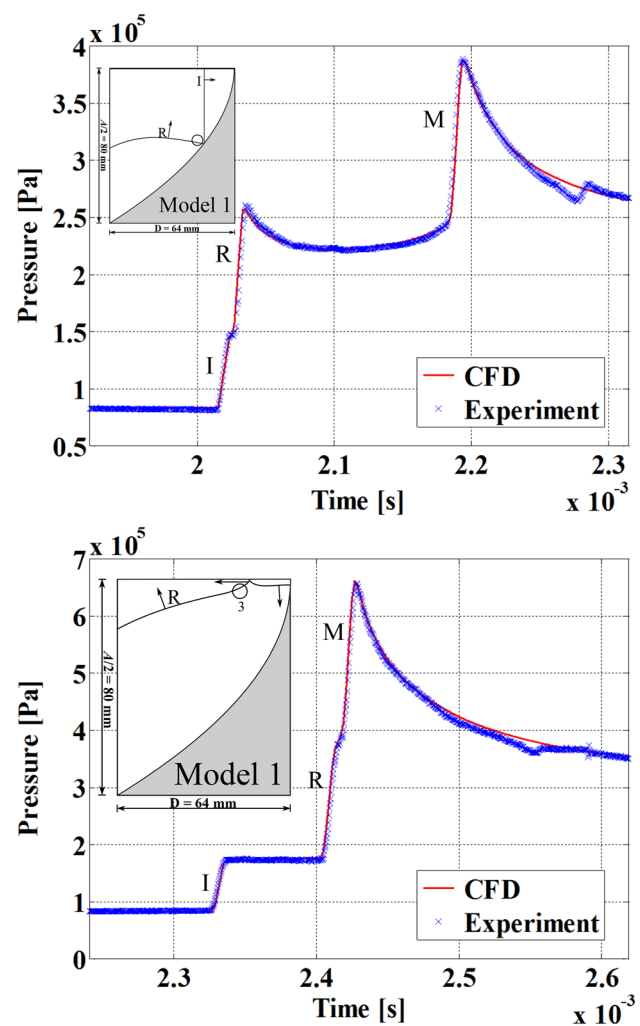

Fig. 7 Comparison of CFD and experimental traces at shown transducer position. The shock Mach numbers were 1.3 (top) and 1.4 (bottom). Atmospheric pressure was 83 100 Pa. Inset image shows the model, the location of the transducer and the wave at a particular instant. Note the finite size of the pressure transducer relative to the size of the flow features

given earlier. I is the incident wave, R the reflected wave off the wall and M the main reflected wave exiting the cavity. There is a slight difference in the traces post-focus with a small jump in the pressure trace which is due to a weak transverse wave in the shock tube. Good agreement returns thereafter.

4 Results for the base case

The vast majority of past investigations has used either parabolic or cylindrical cavities. Interferograms for many of these are given in Takayama (2019). Consider first the weak shock case which has received very little attention in the past, other than a brief coverage in Skews and Kleine

Fig. 9 Direction-indicating colour schlieren showing the development of the jet. Cylindrical cavity. M = 1.23 (top) and 1.35 (bottom). Online resource video1
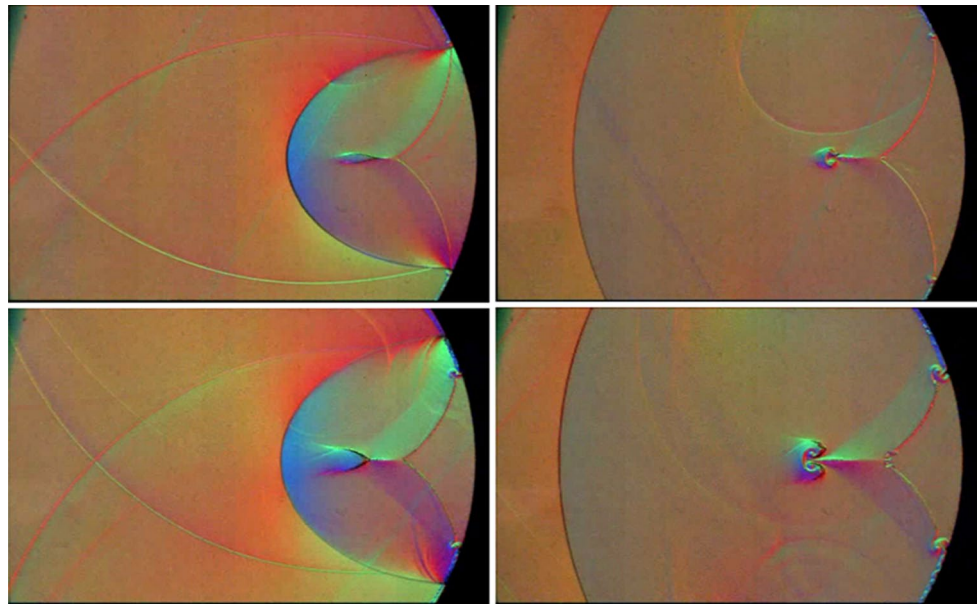
(2007) and Skews and Kleine (2009). Four frames showing this process are given in Fig. 8. The overall pattern is similar to that of the stronger shock in Figs. 4 and 5 except the shear layers are weak and almost indistinguishable, and the focal region is slightly different.

The case of stronger shocks in a cylindrical cavity has been treated in detail in Skews and Kleine (2007), using a suite of greyscale images. The cavity used in these tests has a radius of 64 mm and a depth-to-aperture ratio of 0.5. Of particular note is the post-focus development of the reflected wave and the jetting that occurs. Colour imaging is helpful in assessing the flow. Figure 9 compares features using direction-indicating colour schlieren for Mach numbers of 1.23 and 1.35, showing the features in similar positions. Comparing the final frame in Fig. 8 with the first two frames in Fig. 9 clearly shows the effect of incident shock Mach number. Where the shear layers meet the wall, relative to the foot point of the reflected shock, they move inward with increasing Mach number, and the shear layer termination on the wall becomes more unstable. The jet becomes stronger and terminates in rolled-up vortices. Further description is given in Skews and Kleine (2007).

Interpretation of the flow is enhanced with the use of shearing interferometry. Figure 10 gives a result for a Mach number of 1.35, showing the evolution, with focus
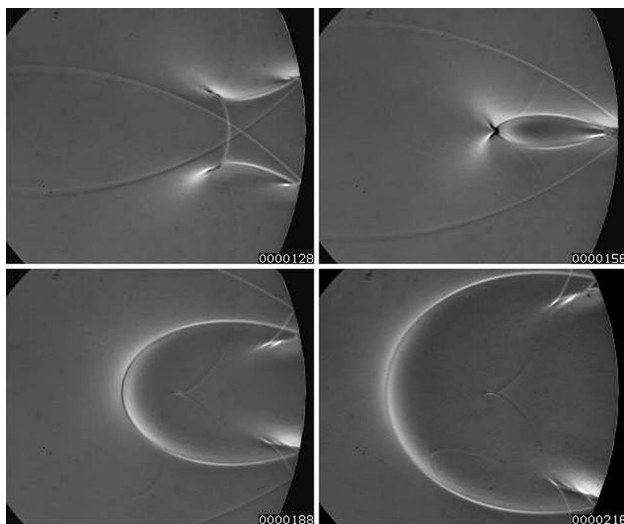
Fig. 8 Mach 1.04 shock in a cylindrical cavity showing pre-focus, focus and post-focus. Omnidirectional schlieren images. Instant of shown flow field (in μs) is indicated on the bottom right corner of each frame
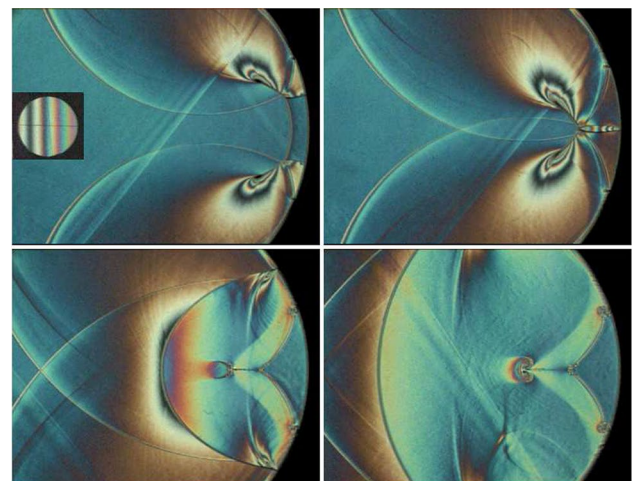
Fig. 10 Shearing interferometer images of the interaction of a Mach 1.35 shock wave; cylindrical cavity
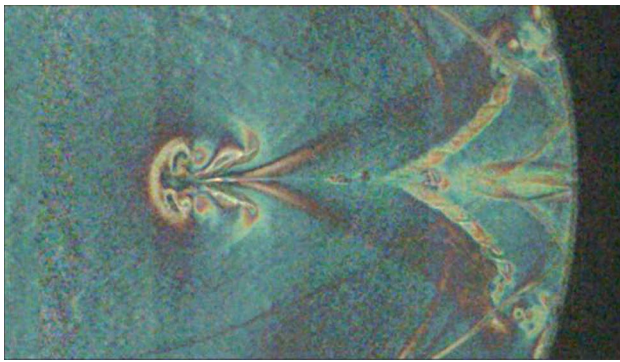
Fig. 11 Detail of the structure at the tip of the jet

Fig. 13 Mach 1.04 shock in a parabolic cavity of depth-to-aperture ratio of 0.5. 32 µs between frames showing pre-focus, focus and post-focus. Omnidirectional schlieren. Online resource video2
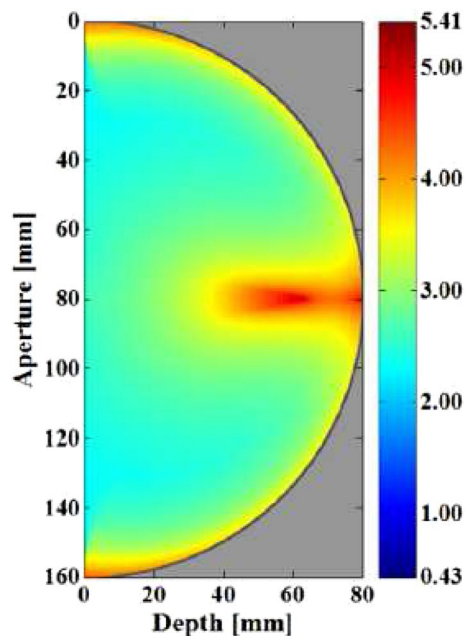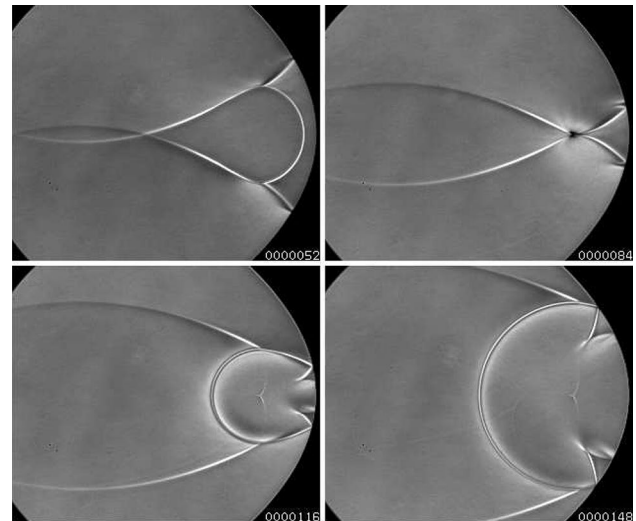

Fig. 12 Map of maximum pressure amplification history for a Mach 1.45 incident shock in a cylindrical cavity. Pressure is normalized with respect to pressure P_2 behind the incident shock

occurring in the second frame. The inset in the first frame is a calibration image taken through a long focal length lens with a vertical fringe arrangement. It assists in interpreting the horizontal gradients in the images. With regard to the development of the reflected wave, in the first frame, it is noticeable that a large gradient occurs on its outer side. By comparing this with the first frame in Fig. 5, it is evident that the compression waves arising from the earlier part of the cavity do not influence the reflected wave as much as those from higher up the curve. Of particular note is the sensitivity of this technique, shown by the clear identification of the features compared to other techniques. Previous work Skews and Kleine (2007) has shown that the jet terminates

in a mushroom-shaped vortex flow. A magnified image taken at a later time (Fig. 11) shows a much more complicated structure with multiple vortex elements, as well as developed Kelvin–Helmholtz instabilities on the shear layers.

In view of the properties in the cavity changing significantly in time and space, it is of interest to establish those regions where maximum values are attained. Thus, during the numerical runs pressure values are saved at each point and the maximum values stored. Figure 12 gives the result for a Mach 1.35 shock in a cylindrical cavity. The focal region is quite broad, extending all the way from the rear part of the cavity where the jet starts to develop up to the main point of focus, corresponding to the second image in Fig. 10. The high pressures along the wall due to the strong Mach stems from the early Mach reflections are evident.

There has been less detailed attention to wave dynamics in a parabolic cavity comparable to that in Skews and Kleine (2007) for the cylindrical case. However, there are some similarities for the same depth-to-aperture ratio, i.e. 0.5, but some marked differences. The case of a very weak shock in a parabolic cavity is given in Fig. 13, also treated very briefly in Skews et al. (2007). This should be compared with Fig. 8 which is for the same Mach number in a cylindrical cavity.

As noted before, the corner signal in the cylinder case does not contribute to the focus, but the lip shocks, which are the shocks that arise from the reflection of the incident shock off the angled leading edge of the test piece, do for the parabolic cavity. The focus also occurs much closer to the base of the cavity. The main reflected shock interacts with the wall as a transitioned regular reflection before being overtaken by the lip shock, and the reflected shock has a

Fig. 14 Mach 1.34 shock interacting in a parabolic cavity of depth-to-aperture ratio of 0.5. 176 μs between frames. In the left frame, four different shear layers (1–4) are indicated. Omnidirectional schlieren. Online resource video3

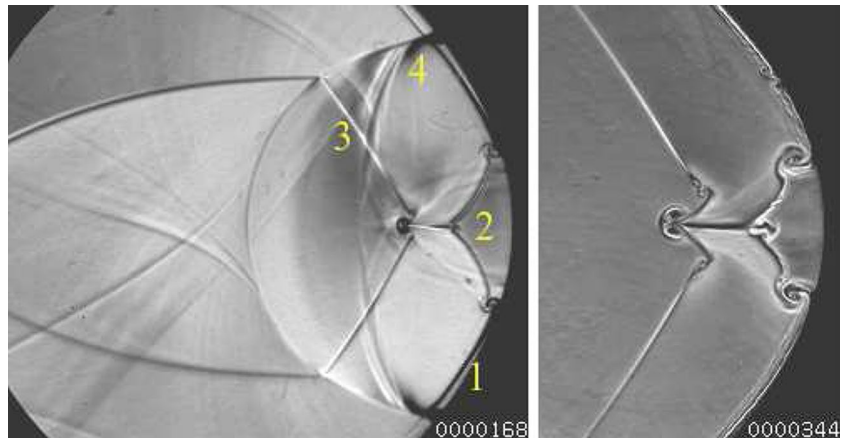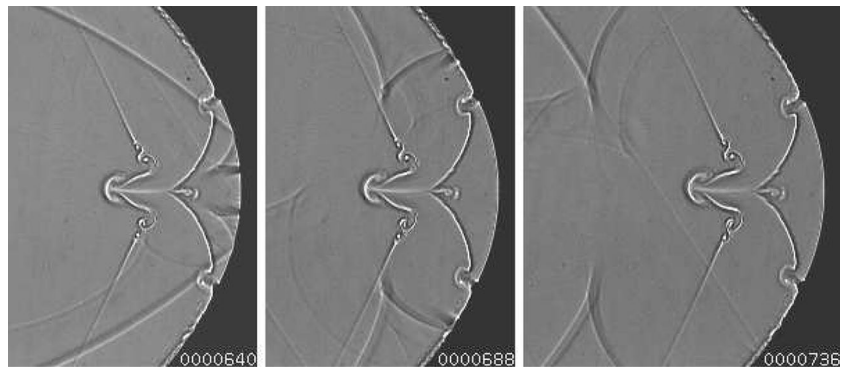**Fig. 15** Mach 1.24 shock in a parabolic cavity of depth-to-aperture ratio of 0.5. Shadowgrams, 48 μs between frames

much rounder profile. The shear layers forming the jet are consequently much less inclined.

The main difference for a stronger shock (Fig. 14), to be compared with Figs. 9 and 10, is the influence of the lip shock. This results in the development of an extra shear layer running from where the lip shock meets the main reflected wave up to the tip of the jet. It develops subsequent to when focusing occurs. There are thus four different shear layers in the flow field (indicated by yellow numbers in the figure): the first from the initial reflection off the surface, the second resulting from focus, the third due to the lip shock interaction with the reflected wave and the fourth from the triple point when the main reflected shock reflects off the surface. This shear layer is difficult to discern on individual frames and is generally only identified in animations. The second frame shows the flow at a later time. Other than the new shear layer similar complex jetting occurs as in the cylindrical case, with instability on the shear layers. It should also be noted that the flow field has become considerably more uniform, with larger density gradients only appearing in the vicinity of the discontinuities.

A further feature can occur, such as shown at an intermediate Mach number in Fig. 15. As the lip shock moves outwards away from the main reflected wave, it reflects off the cavity surface in a transitioned regular reflection which
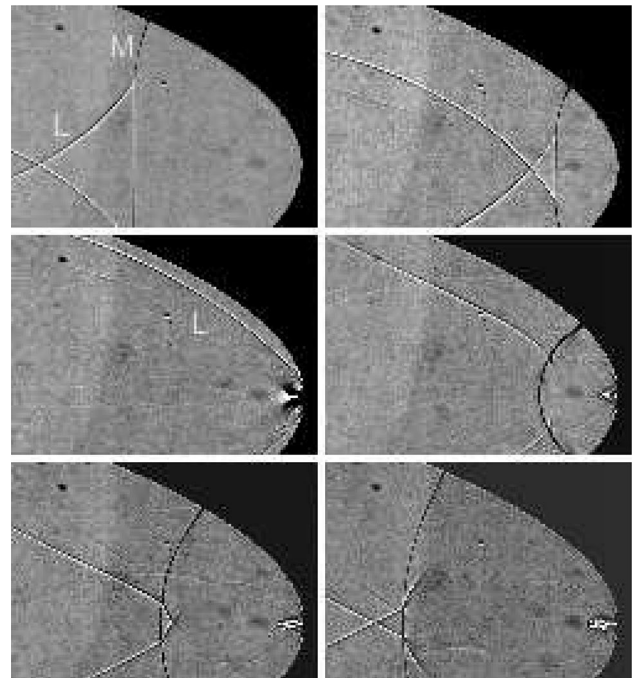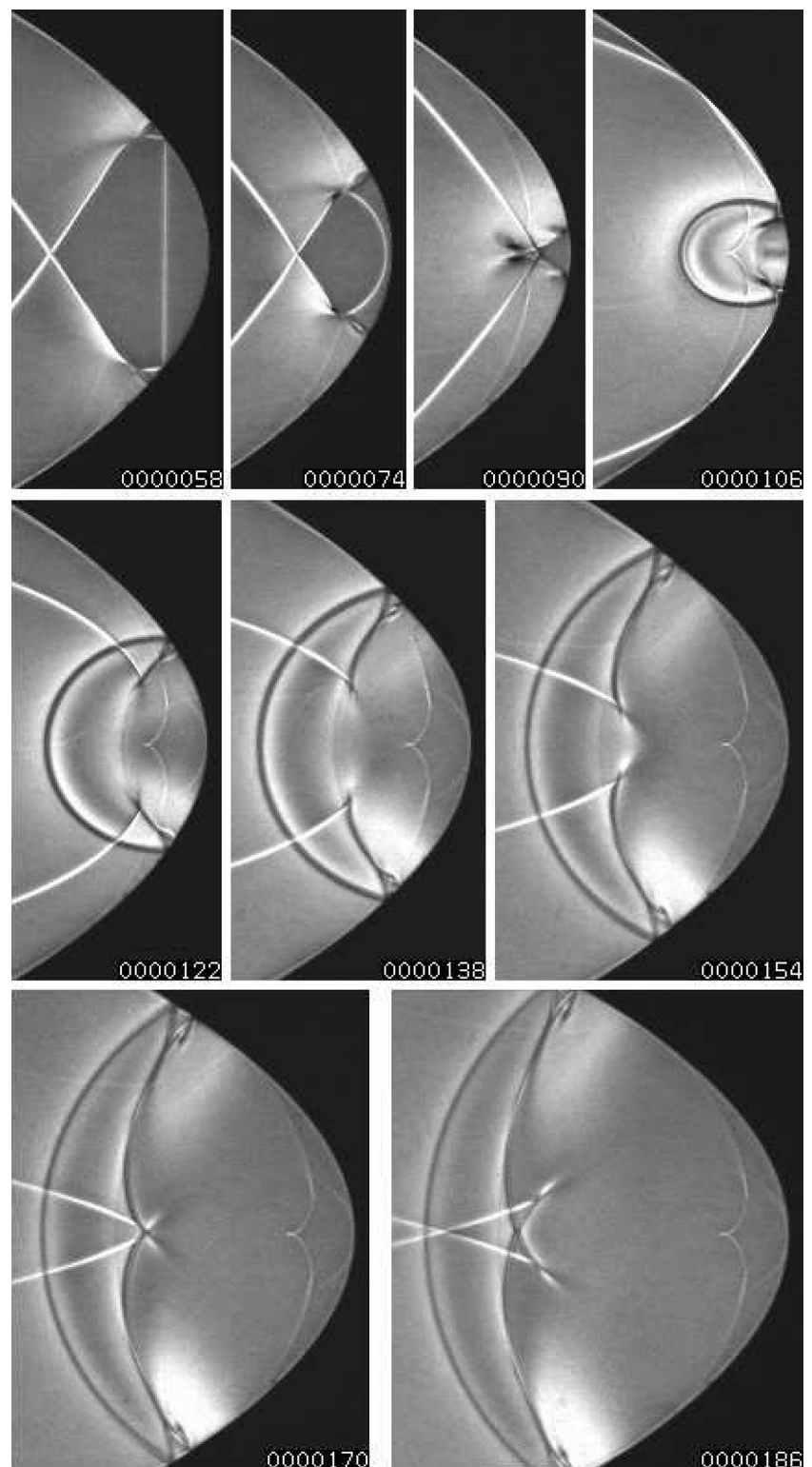
Fig. 16 Shadow images of a Mach 1.23 shock in a parabolic cavity of depth-to-aperture ratio of 1.0. Time between frames 80 μs

Fig. 17 Schlieren images of a Mach 1.05 shock in a parabolic cavity of depth-to-aperture ratio of 1.0. Time between frames 16 μs

then also propagates out of the cavity. What is particularly noticeable is that in the nearly 100 μs between the first and last frame the complex flow at the base does not move. Extending the time confirms that the conditions at the base of the cavity are almost stationary.

Deeper parabolic cavities have hardly been examined before. It is helpful to follow the behaviour of the lip shock before examining the complex flow at the apex. Figure 16 shows part images of a Mach 1.23 incident shock in a parabolic cavity with a depth-to-aperture ratio of unity. Because

of the shallowness of the surface entry angle, reflection starts as a Mach reflection, M, with a highly curved Mach stem. They propagate from either side up to the focus region, shown in the third frame. The lip shock, L, then reflects off the wall of the cavity and propagates inwards intersecting with the main reflected shock, resulting in a transmitted wave. The two reflected lip shocks then cross in front of the reflected wave and result in Mach reflections on the main reflected wave. It is clear from these images that the region of focus is very small and complex.

It is evident that the behaviour at the apex is of interest. This is examined, starting with a weak incident shock in Fig. 17. The initial Mach reflection transitions to a regular reflection further into the cavity with the reflected wave interacting with the lip shock as shown in the first image. After reflection from the base of the cavity, a highly curved reflected wave results, also interacting with the lip shock resulting in a wall shock and the development of a shear layer. This layer subsequently combines with the one from the other side forming focus and a jet. This is entirely different from the jet formation in the cylindrical case. This does not occur when the lip shocks meet on the axis, but when the wall shocks intersect, followed by the development of the main reflected wave, as in the fourth frame. At this stage, the lip shocks reflect off the surface and propagate inwards. The lip shocks then propagate through the main reflected wave and meet the main reflected wave's reflection from the surface, in a rather complex manner appearing to consist of a number of waves. The first image in the last row shows the meeting of the reflected lip shocks and those coming off the wall, in a focus followed by a diverging interaction.

Increasing incident shock strength gives some overall flow features that are similar to the weak case, but there are many significant differences, particularly near the apex, as shown in Fig. 18. The lip shocks, R, cross and the part approaching the surface reflect as a Mach reflection, H, which because of the sensitivity of the schlieren system shows up as a dark patch. The stem is so strong that a series of wavelets are generated behind it because of

Fig. 18 Schlieren images near the apex of a Mach 1.22 shock in a parabolic cavity of depth-to-aperture ratio of 1.0. I is the incident shock, R a lip shock, H a Mach reflection and M the main reflected wave. Time between frames 6 μs
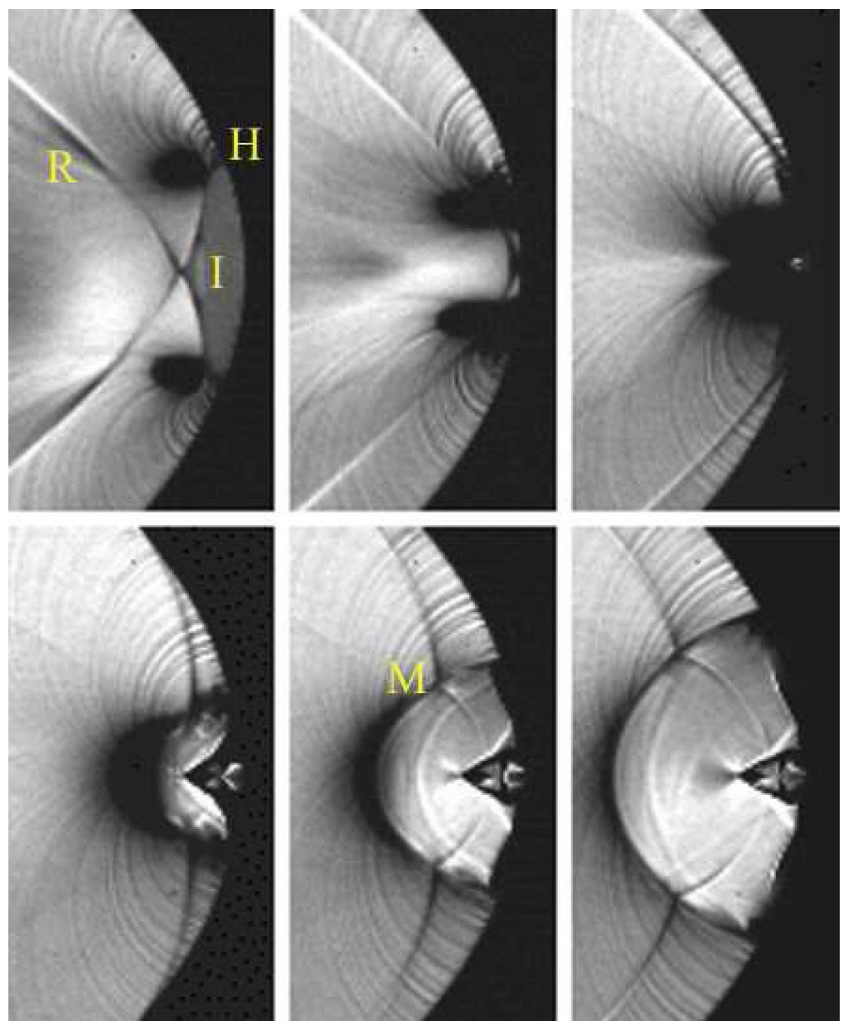
Fig. 19 Schlieren images of a Mach 1.22 shock in a parabolic cavity of depth-to-aperture ratio of 1.0. Instant of shown flow field (in μs) is indicated on the bottom right corner of each frame
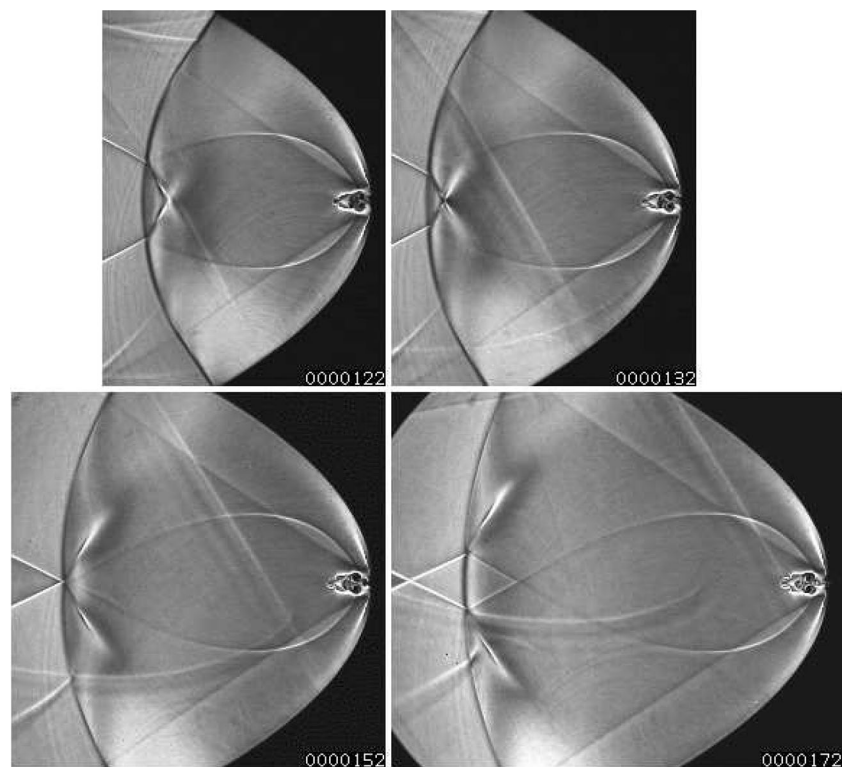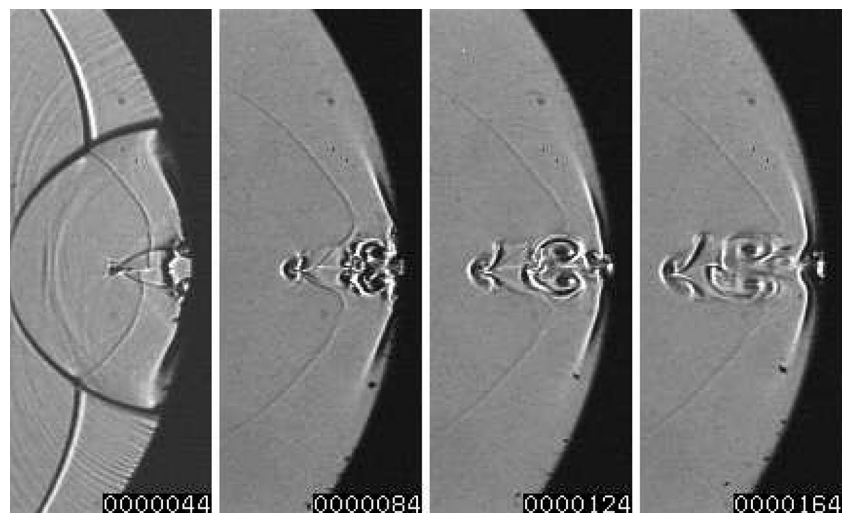
Fig. 20 Shadow images of a Mach 1.22 shock in a parabolic cavity of depth-to-aperture ratio of 1.0. Time between frames 40μs

the slight roughness of the surface, as evident in the first frame. Although not visible in the second image, closer study indicates that the incident wave may be overtaken by these stems before it strikes the back of the cavity. Focus occurs in the third frame. Subsequent frames show the development of the main reflected wave, M. In the fourth frame, the lip shock reflects off the surface and thereafter propagates inwards. The last two frames show the development of shear layers where the lip shock meets the main reflected wave. Further evolution is shown in Fig. 19. In the first frame, the lip shocks meet behind the reflected

shock with a reflected wave still trailing the shear layers. The features all meet in the second frame generating a second focus. The shear layers meet, enclosing a fixed mass of gas. The lip shocks then move apart with a continuation of the shear layers and reflection patterns. The jet at the base of the cavity remains small, and using shadowgraph images is shown in more detail in Fig. 20. As in the case of a cylindrical cavity, the tip has a mushroom shape, but a stronger complex vortex pattern is produced closer to the base. The shape of the shear layers arising from the lip

Fig. 21 Shadowgraph images of a Mach 1.34 shock in a weighted catenary cavity, depth-to-aperture ratio 0.714. Top row at 6 µs between frames and bottom row every 12 µs later
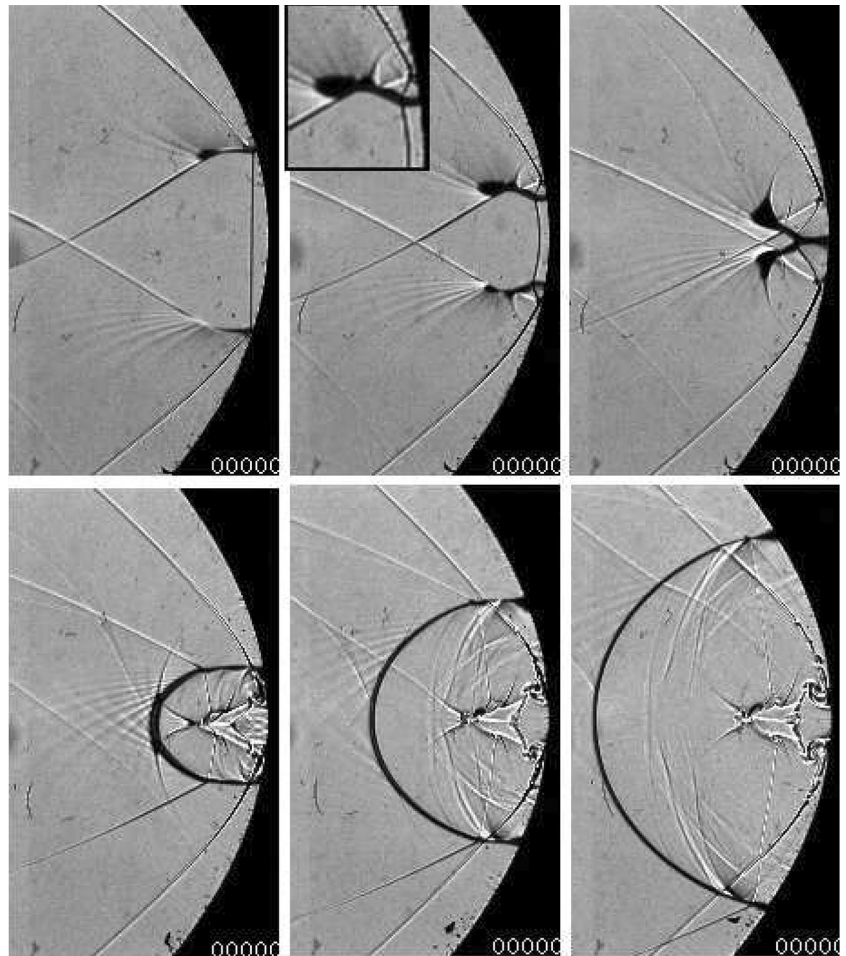

shock interaction with the main reflected wave is strongly influenced by the flows near the jet.

Some results for a variety of cavities with profiles not having been used previously are given in the next section.

5 Non-standard and compound cavities

Studies have shown the differences between a parabolic profile and a weighted catenary are very small for the same depth-to-aperture ratio (MacLucas 2012), and thus, flow features are very similar and can be compared. A

Fig. 22 Air velocity vector plots superimposed onto interferometry images. Vectors are scaled and coloured according to their resultant magnitude measured in the laboratory frame of reference. Numerical interferogram
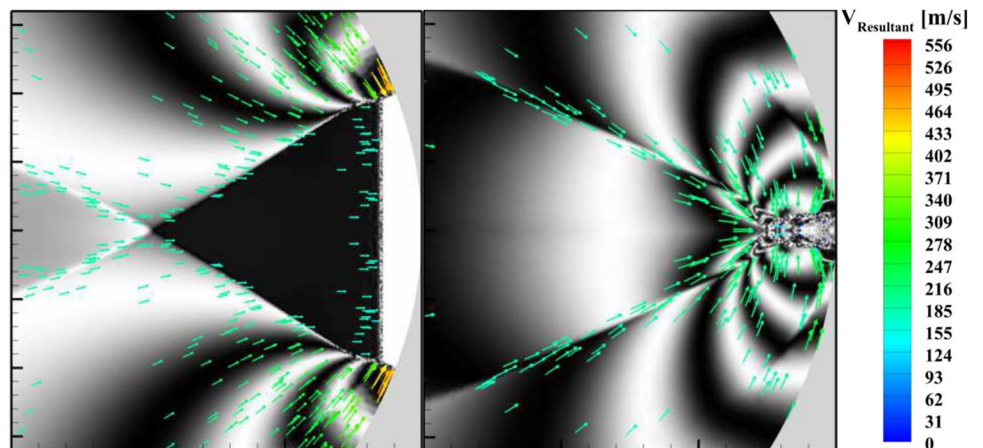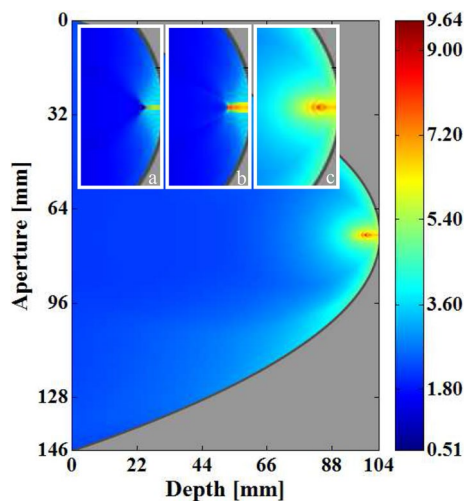
Fig. 23 Maps of maximum pressure amplification history. Inset images **a** and **b** illustrate pressure amplification at the start of focus. Image **c** is an enlargement of the focal area of the final history map. The time differences between inset images are 2 μs and 274 μs, respectively. Pressure is normalized with respect to pressure P_2 behind the incident shock wave. Incident shock Mach number is 1.34

comprehensive experimental and numerical study using a weighted catenary of depth-to-aperture ratio of 0.714 and equation $x = 1 - \cosh 6.2y$ has been conducted at a Mach number of 1.34 using a selection of techniques. These can be compared with the corresponding parabolic results at Mach 1.22 in Fig. 18. There are significant differences. In the weaker case, the extension of the lip shock, R, forms a Mach reflection, H, at the surface, whereas in the stronger case (Fig. 21) compressions from the wall cause a Mach reflection much further away from the surface. In the second frame, the incident shock has reflected off the base of the cavity resulting in a complex reflection pattern as shown in the inset. Focus occurs in the third frame. Thereafter, the main reflected wave develops with a complex jet at the base of the cavity, of different shape to that for the lower Mach number.

The experimental test case above was simulated numerically, and the numerical data were converted to an interferogram with the fringes corresponding to conditions of constant density. The first frame in Fig. 22 clearly shows the concentration of density on the lip shock resulting in the development of a Mach reflection. Also plotted are the velocity vectors, which clearly show the very high velocity induced behind the strong Mach stem at the wall. The air velocity magnitude behind the Mach stem is larger than that behind the reflected wave, as expected. The difference in velocity between these two areas increases as the Mach reflection reaches the base of the profile. The second frame shows conditions near focus with all the velocity vectors
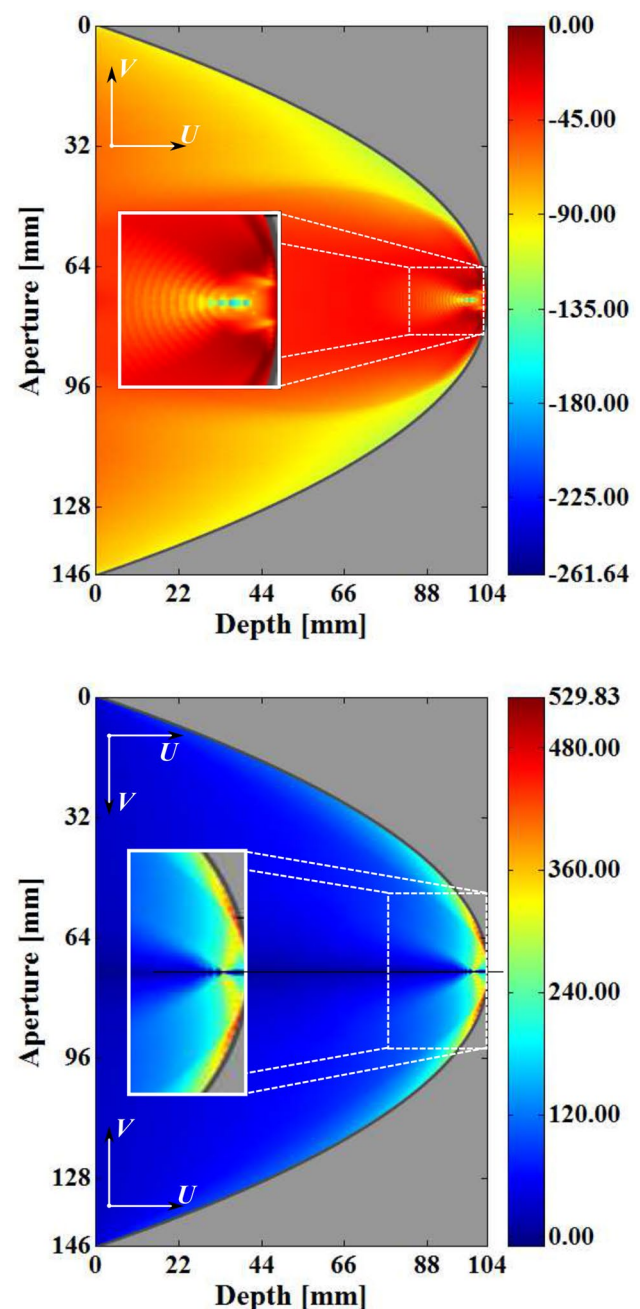

Fig. 24 Top image: minimum U velocity (m/s) history. Bottom image: maximum V velocity (m/s) history

converging on the focal region, as well as an indication of flow starting to move away from the base.

Figure 23 shows the maximum pressure history map for the weighted catenary cavity at different times. The increase in the magnitude and extent of the focal region with time are clear, as is the distance of highest pressures from the base of the cavity.

Similar evaluations of the cavity flow regarding velocity are given in Fig. 24. The left-hand plot shows the minimum
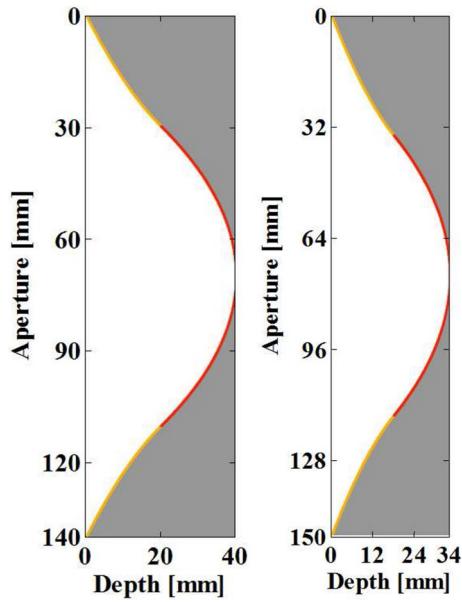
Fig. 25 Experimental compound profiles A and B. Yellow: inlet, red: reflector

Table 1 Experimental test pieces. For compound profiles, the reflector aperture is the aperture of the base reflector curve, and similarly, the inlet aperture is the aperture at the extent of the inlet profile; the inlet aperture is also the aperture of the entire model

Model	Reflection aperture (mm)	Inlet aperture (mm)	D/A
A	40	140	0.287
B	40	149.5	0.226

horizontal component of velocity, U, negative in view of the flow being out of the cavity, and tending to zero near the base of the cavity as the flow stagnates. On the other hand, the maximum vertical velocity, V, zero on the axis, reaches very high values, in excess of 500m/s, due to the Mach stem of the Mach reflection at the surface. It then reduces along the shear layer up to the point of focus on the axis.

An important contribution is that of Babinsky et al. (1998). This dealt with compound profiles and showed that having a shaped inlet at the entrance to the main cavity resulted in significant increases in focusing pressure. The cavities were restricted to cylindrical profiles for both the inlet and the base cavity shape. This led to the current more comprehensive study of compound profiles, two of which have been evaluated from the point of view of wave patterns. The experimental profiles are shown in Fig. 25. The first consisted of a weighted catenary main cavity with parabolic inlets and the second with both parts being parabolic. The main reflection curve is identified with a red line and the inlet curve with yellow. Specifications are given in
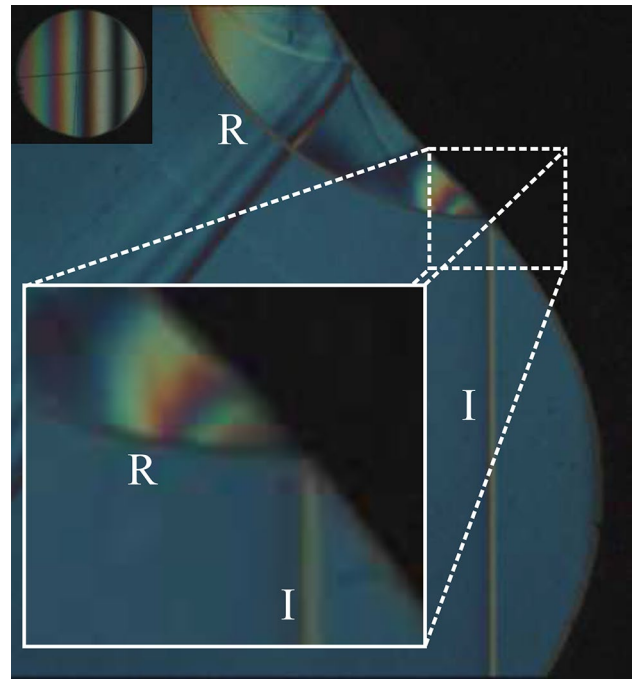

Fig. 26 Initial reflection of the incident shock wave with compound model A. The incident shock wave has a Mach number of 1.44. Online resource video4, for the next four figures
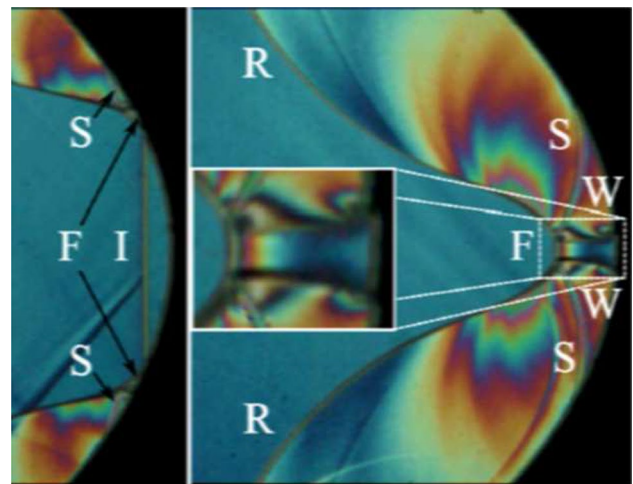

Fig. 27 Development of shock system pre-focus. M = 1.44. Continuation of process shown in Fig. 26 (same experiment using shearing interferometry)

Table 1. The shapes chosen were to approximately represent the shock from a high-level blast approaching ground topography of hills and valleys. An overview of the wave systems for the first case has been described in MacLucas et al. (2015) using shadowgraphy and direction-indicating schlieren imaging, but not as regards pressure distributions.
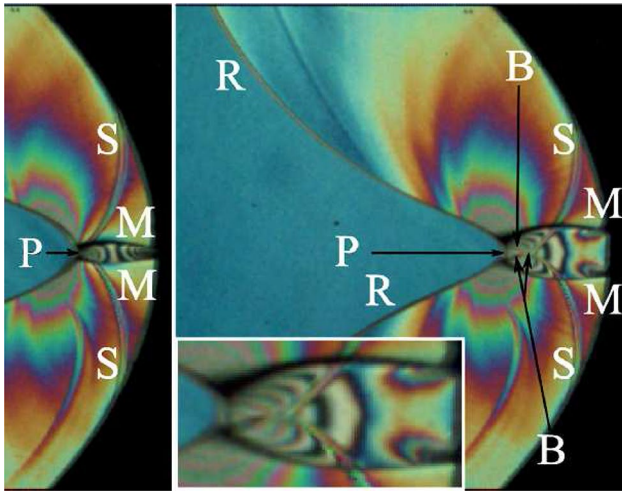
Fig. 28 Progression of gas dynamic focus. The time difference between the frames is 6 μs. Continuation of process shown in Fig. 26 (same experiment)

Fig. 30 Post-focus shock wave behaviour. Continuation of process shown in Fig. 26 (same experiment)

The initial engagement of a plane shock wave with these models results in a regular reflection due to the blunt entrance of the inlet although the angle between the incident wave and the surface increases as the wave enters the cavity. This is shown in Fig. 26 for model A using shearing interferometry, with a colour coding as in Fig. 10. Note that weak transverse waves trail the incident shock wave. These waves can distort the fringes in an area of interest, but are weak and can be neglected. Higher-order fringes develop behind the reflection point decreasing in order away from the reflection point and can be shown from simulation to be an expansive region. The following figures up to Fig. 30 are from the same test.

Fig. 29 Left image illustrates the end of gas dynamic focus followed by post-focus wave development. Time between frames 64 μs. Continuation of process shown in Fig. 26 (same experiment)
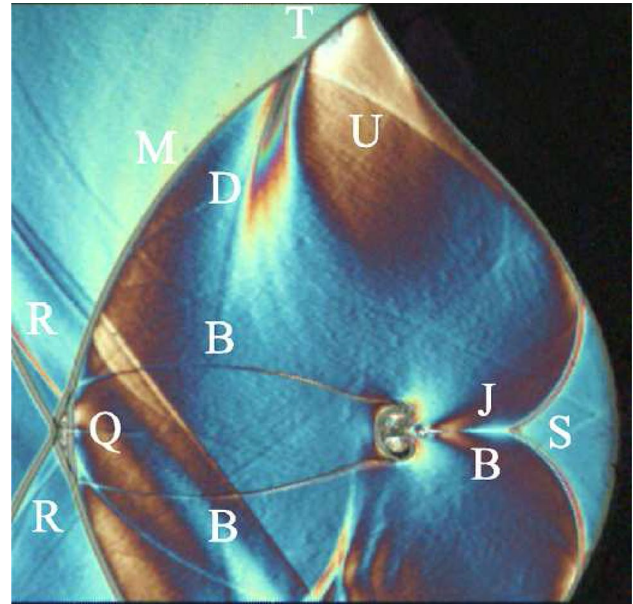
Figure 27 shows a slightly later stage when the incident wave moves into the concave portion of the profile. The left-hand image shows the reflection off the wall becoming a transitioned regular reflection, TRR, with a shear layer, S, and reflected wave, F, which then join after the incident wave has fully reflected, as shown in the right-hand image. The wall shocks from the TRR then approach each other before they collide forming start of focus.

The left-hand image in Fig. 28 illustrates the start of gas dynamic focus and of the main reflected wave, M. The triple points of the two Mach reflections have reflected off each other along with the wall shock. A new set of Mach reflections is formed – the Mach stem, P, from waves R and M and a new barely visible shear layer B, developed behind the Mach stem in the focal region. This is identified more clearly in the inset.

The end of focus occurs when the two reflected waves meet on the axis with the main reflected wave as shown in the left image in Fig. 29. The focal region is enclosed by the shear layers, B, developed from both ends of the Mach stem P where they meet the earlier shear layers, S. Areas of stagnation or near stagnation occur behind these shear layers and in areas adjacent to the focal region. However, this latter area will tend to shift as the expansion field continues to evolve with the propagation of M. Interestingly, the interaction of M with the profile wall overtakes these shear layers as shown in Fig. 29. With the crossing of the reflected shocks, R, a Mach reflection, Q, develops with two trailing shear layers, B, as illustrated in the right-hand image.
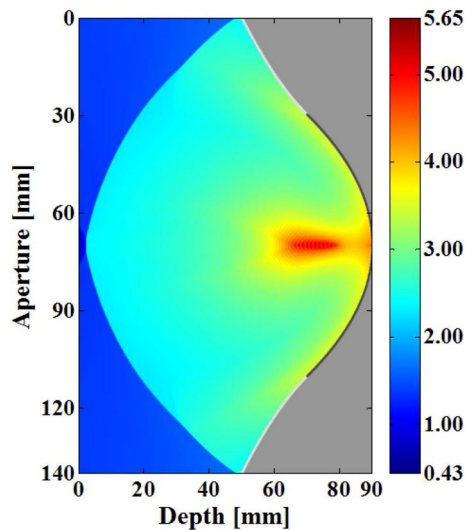
Fig. 31 Map of maximum pressure amplification history for a Mach 1.45 incident shock in cavity model A. Pressure is normalized with respect to pressure P_2 behind the incident shock

The post-focus wave behaviour, illustrated in Fig. 30, shows an expansion of the main reflected wave, M, along with a slight enlargement of the Mach stem Q. The expansion field behind M continues to weaken as noted by changes in fringe colour compared to those in Fig. 29. The field in front of M has been severely attenuated as indicated by the change in colour. As the main reflected wave M proceeds to exit the profile, a Mach reflection of M with the profile wall develops, consisting of the Mach stem, T, the reflected shock wave, D, and shock wave, M, along with a new shear layer, U. The initiation of the reflection appears to occur where the inlet and reflector portions of the profile meet, resulting in a non-uniform expansion behind the Mach stem T.

Some of the properties of this compound cavity are given in Figs. 31 and 32. Peak pressure amplification occurs in the focal region behind and near the Mach stem. It can also be shown that the extent of the peak pressure region increases along with the peak pressure amplification with increasing Mach number. It is noted that the peak pressure is similar in magnitude to that in a cylindrical cavity (Fig. 12), but in a cavity just above half the value of depth-to-aperture ratio, clearly indicating the influence of the inlet profile.

Some experiments have been conducted on the shallower compound profile, labelled B in Fig. 25, having an even smaller depth-to-aperture ratio. Experiments were conducted using schlieren photography giving better shock wave definition compared to shearing interferometry due to the latter's inherent property of double imaging. The first frame in Fig. 33 shows the incident wave reflecting off the convex surface of the profile in a regular reflection. The corner signal behind the reflection point is clearly visible, as is a weak transverse wave which does not influence the interaction. In
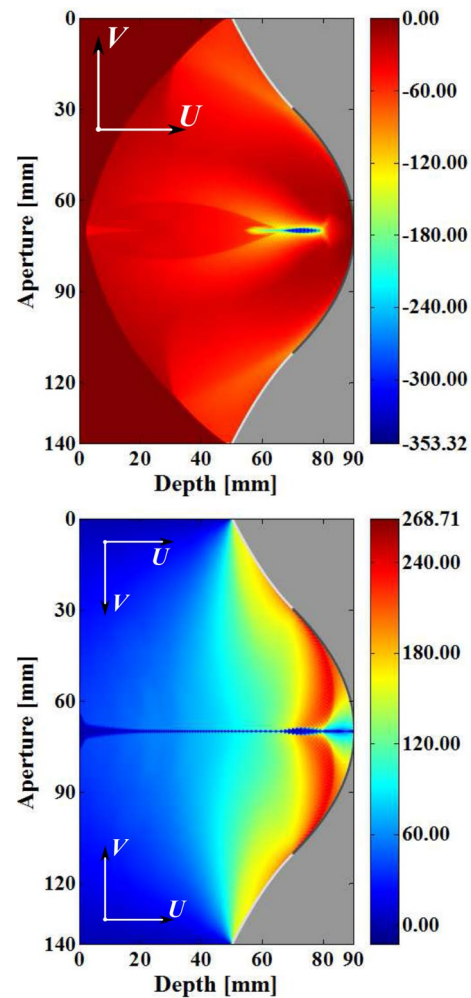

Fig. 32 Top image: minimum U velocity (m/s) history in cavity model A. Bottom image: maximum V velocity (m/s) history

the second frame the reflection has become a transitioned regular reflection with a reflected wave, F, and wall shock, W. The shear layer resulting from the interaction between waves F, W and R is not visible in the image reproduction. Thereafter, the incident wave, I, being fully reflected from the base of the profile two Mach reflections develops, from either end of the model, consisting of the shared Mach stem, F, and reflected waves, R and W, as seen in the third frame. The corner signal remains visible.

In Fig. 34, the two triple points have met on the centre line of the cavity initiating focus and main reflected shock M. The wall shocks have reflected off each other and have darkened considerably which indicates an increase in shock strength, and in the second frame, a new Mach stem P is visible in the focal region, developing shear layers B in its wake. In the last frame, gas dynamic focus is complete with the crossing of the reflected shocks R, thereby enclosing the focal region within shear layers B developed from

Fig. 33 Pre-focus engagement of an incident shock wave of Mach 1.34 with model B using schlieren photography. Time differences between the individual frames are 36 µs and 44 µs, respectively
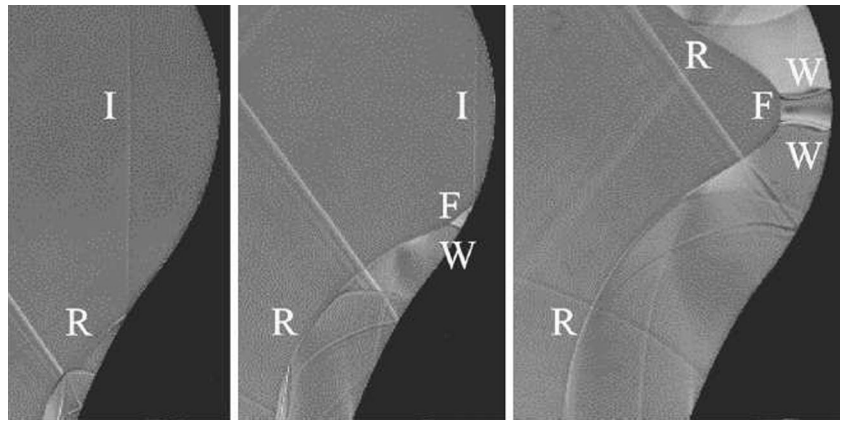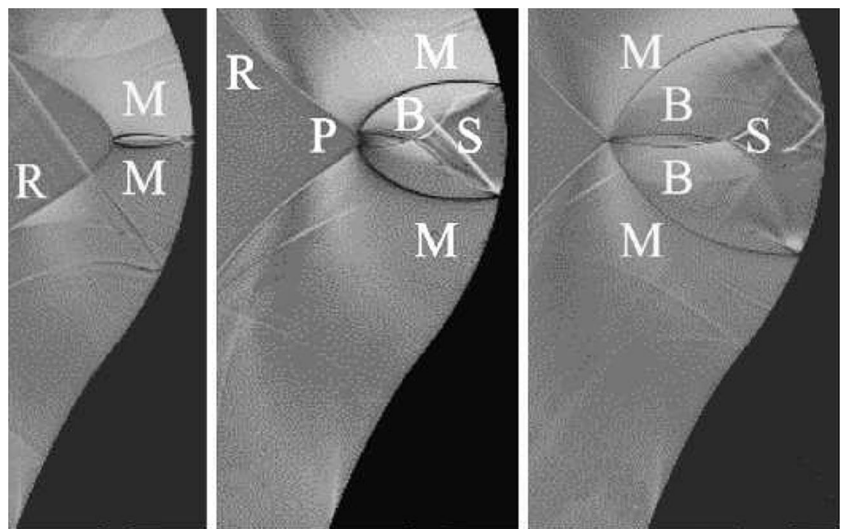
Fig. 34 Gas dynamic focus of the incident shock wave. Mach 1.34 with model B. The time difference between frames is 24 µs schlieren imaging

each Mach reflection, with the original shear layers S. This structure is significantly different from the jet formation in a cylindrical cavity.

This difference is even more marked with later evolution as shown in Fig. 35. This illustrates the development of a new Mach stem Q with shear layers B developed from either end of the Mach stem. Interestingly, the main reflected wave, M, overtakes the reflected waves, R, developing a new Mach stem V. The double crossing of the shear layers B is clearly visible where the Mach stem V has significantly enlarged as in the lowest frame. The shear layers B in the focal region start to develop Kelvin–Helmholtz instabilities. This triple crossing has not been observed before and illustrates the nonlinear effects at play. The situation is also somewhat different for a weaker shock, as shown in Fig. 36, where a single shear layer, B, is visible in the focal region.

The map of maximum pressure amplification history is shown in Fig. 37. The effect of the shallower profile compared to the similar compound profile in Fig. 31 is a more diffuse and extensive focal area as well as a decreased peak

pressure, as is to be expected. The corresponding velocity maps are given in Fig. 38. There is a significant reduction in the velocity components, particularly in the focal area.

6 Additional profiles

In view of the excellent agreement between the numerical simulation and experiment for the cavity profiles introduced in the preceding sections, some additional profiles have been explored using simulation. Numerical interferograms and maximum pressure history plots are used for comparison.

6.1 Elliptical profiles

Three elliptical profiles of depth-to-aperture ratios of 0.25, 0.5 and 0.75 were evaluated, with the 0.5 case corresponding to a cylindrical cavity. The other two are shown in Fig. 39.
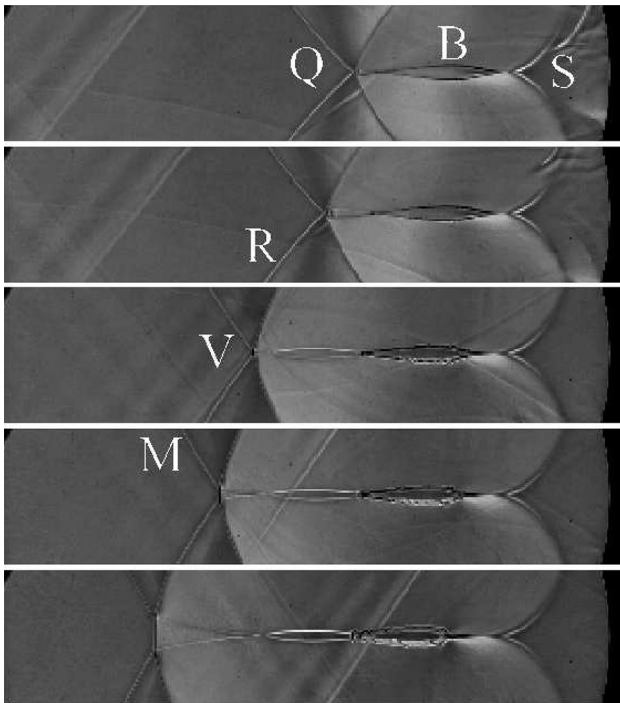
Fig. 35 Post-focus wave behaviour illustrating the variation in reflection and shear layer patterns. Mach 1.34 with model B. Schlieren imaging
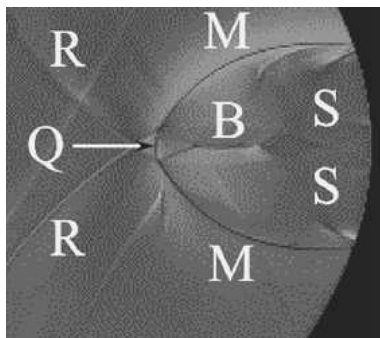

Fig. 36 Post-focus topology for a Mach 1.2 incident shock wave with model B

The initial engagement of a plane shock with a shallow elliptical profile is similar to the interaction in circular profiles. A Mach reflection is developed and then transitions from the direct form to the inverse type and finally to a TRR. These transitions occur rapidly as a result of the quickly increasing slope of the shallow elliptical profile. Thereafter, the triple point of the TRR translates away from the base of the profile enlarging the wall shocks which reflect off each other prior to focus. Focus for the Mach 1.2 case occurs near the entrance of the cavity, and post-focus produces a large Mach stem, P, and shear layers, B, from either end of the
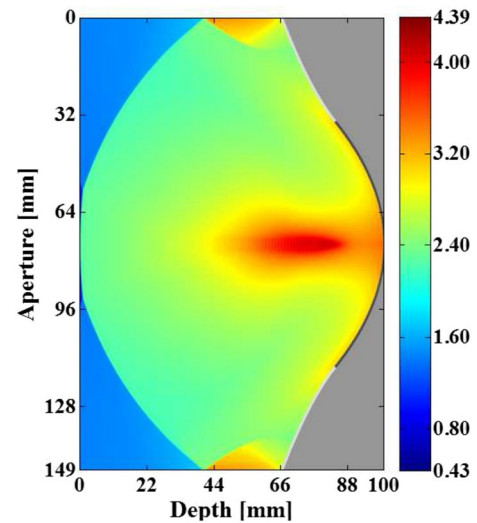

Fig. 37 Map of maximum pressure amplification history for a Mach 1.45 incident shock for model B
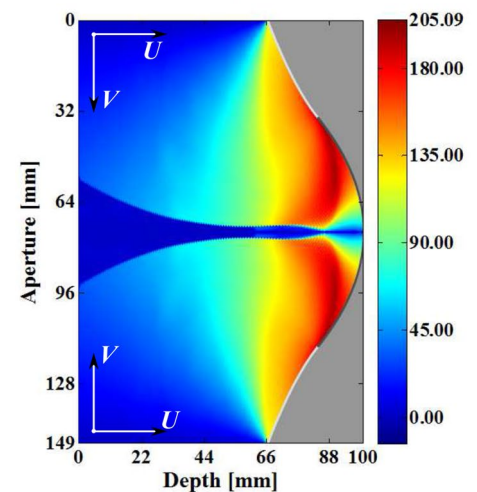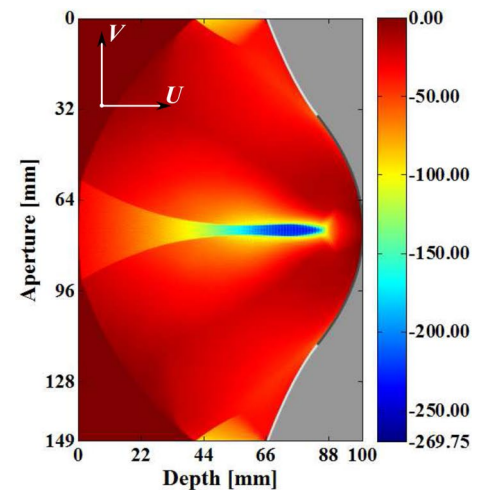

Fig. 38 Top image illustrates minimum U velocity (m/s) history. Bottom image illustrates maximum V velocity (m/s) history
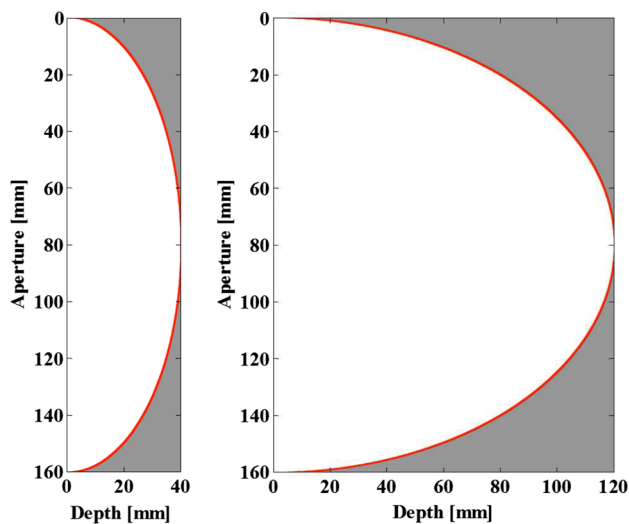
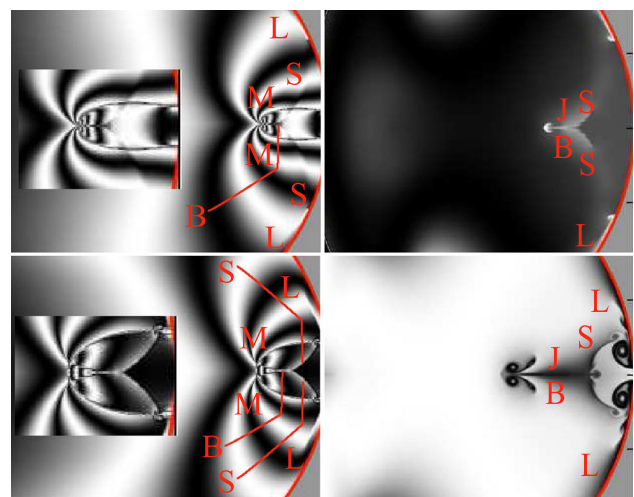**Fig. 39** Two of the elliptical profiles studied

Fig. 41 Numerical interferograms of focus and post-focus wave configurations for depth-to-aperture ratio of 0.75. Incident shock wave M = 1.2 (top) and 1.45 (bottom)
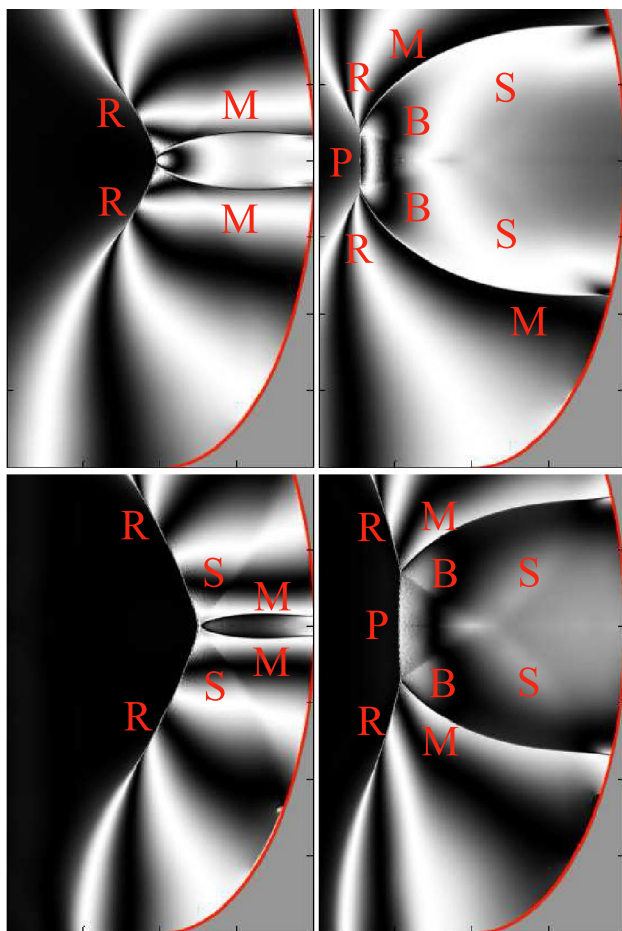

Fig. 40 Numerical interferograms of focus and post-focus wave configurations for an elliptical profile with depth-to-aperture ratio of 0.25. Incident shock wave M = 1.2 (top) and 1.45 (bottom)

stem as shown in Fig. 40. Focus for the Mach 1.45 case is very similar producing a larger Mach stem P that continues to grow in length as the shock system moves away from the cavity entrance. These results indicate that the focus topology is fixed across the investigated Mach number range.

Results for a deeper cavity with a depth-to-aperture ration of 0.75 are given in Fig. 41 at focus and post-focus. At earlier times due to the shallow entry of the surface, no initial shock reflection is formed and the incident shock wave is bent forward by a series of compressions ensuring a perpendicular termination with the profile wall. A stationary Mach reflection is then formed which transitions to the inverse type. Thereafter, a TRR is formed, rapidly followed by a Mach reflection, as previously described for a cylindrical cavity from the shock waves F, R, W and the shear layer. Focus proceeds until the reflected shock wave weakens with the passing of the main reflected wave M in a similar fashion to the shallower profile. New shear layers, S, develop following that from the original Mach reflection, L. The characteristic mushroom-shaped tip of the jet, J, together with the shear layers, B, arising from the interaction of the original reflected wave with the main wave is similar to the case of a cylindrical cavity. Besides the main jet, a rearward facing jet is formed between the shear layers, S. Clearly a point of stagnation exists along the centre line of the profile between the forward jet, J, and the rearward jet.

Maps of maximum pressure amplification history are given in Fig. 42 for the different depth-to-aperture ratios. These indicate that the peak pressure amplification occurs at the start of focus and ends with the weakening of the reflected shock waves, R. The maximum pressure amplification increases with increased profile depth. The area of

Fig. 42 Map of maximum pressure amplification history for a Mach 1.45 incident shock for depth-to-aperture ratios of 0.25, 0.5 and 0.75. The middle frame corresponds to Fig. 12 and is included for comparison purposes
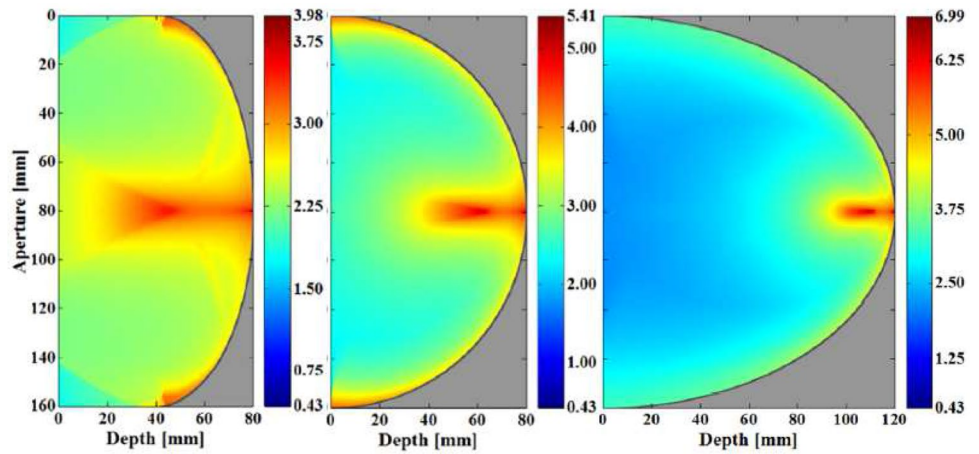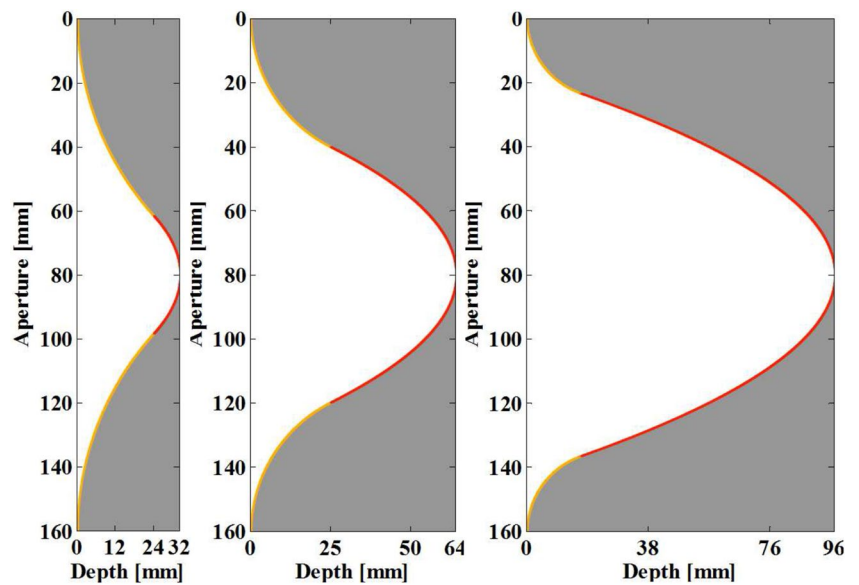
Fig. 43 Compound profiles selected for numerical study. Yellow: inlet, red: reflector

peak pressure amplification reduces with increases in profile depth.

6.2 Compound profiles

As shown earlier, and in Babinsky et al. (1998), the combination of an inlet profile and a reflector profile can have a significant effect on shock focusing. Therefore, it may be possible to produce the focus mechanism found in deep profiles in compound profiles with a smaller depth-to-aperture ratio. In order to test this hypothesis, a circular inlet profile was selected and blended with the deepest pure parabolic reflector. The three compound profiles generated are shown in Fig. 43, having depth-to-aperture ratios of 0.2, 0.4 and 0.6, and are discussed below. There are numerous parameters that can be varied in creating such compound profiles which have not been fully explored, so these results are limited. A certain combination of these would likely cause a

change in focus mechanism. It has been shown Babinsky et al. (1998) that changes in focus mechanism are sensitive to changes in timing of the arrival of the various shock waves in the focal region.

For the compound model with the lowest depth-to-aperture ratio of 0.2, regular reflection persists into the reflector section of the profile. Thereafter, a TRR forms. The pre-focus shock pattern is shown in the top row in Fig. 44, for two Mach numbers. In both cases, a three-shock reflection pattern forms, consisting of the shock waves F, R and W. In the middle row, the system is at focus where the triple points of the three-shock reflection patterns have met on the profile's centre line, characteristic of the standard focus mechanism. The last row of images shows that the reflected shock waves R have crossed (or form a regular reflection that precedes the main reflected wave M). This behaviour differs from elliptical, parabolic and the weighted catenary profiles of similar depth-to-aperture ratios.
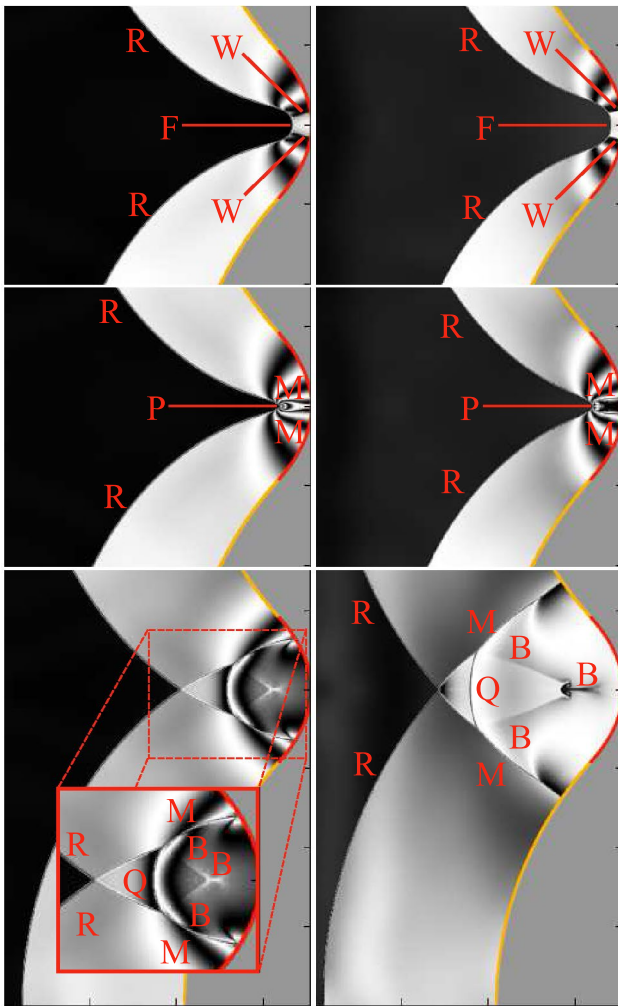
Fig. 44 Numerical interferograms illustrating the pre-focus (first row), focus (second row) and post-focus (third row) shock wave arrangements at M = 1.2 (left column) and 1.45 (right column) for depth-to-aperture ratio of 0.2

For the medium-depth profile, a Mach reflection occurs following the initial regular reflection. No TRR is formed in this case as the full reflection of the incident shock wave occurs; at the same time, the triple point of the Mach reflection arrives at the base of the profile, the Mach reflection having transitioned to the inverse type. The pre-focus shock wave arrangement is illustrated in the first row in Fig. 45 for both Mach numbers. In all cases, the focus mechanism is identical, where a single set of triple points meets on the profiles axis of symmetry. The second row illustrates the start of gas dynamic focus. In all cases, the focus process is quite short, with the reflected shock wave, R, crossing shortly after the triple points have met. In addition, the short duration of focus results in a short centre line shear layer, B, where the vortices formed from the forked section of B and vortices developed on S are in close proximity.
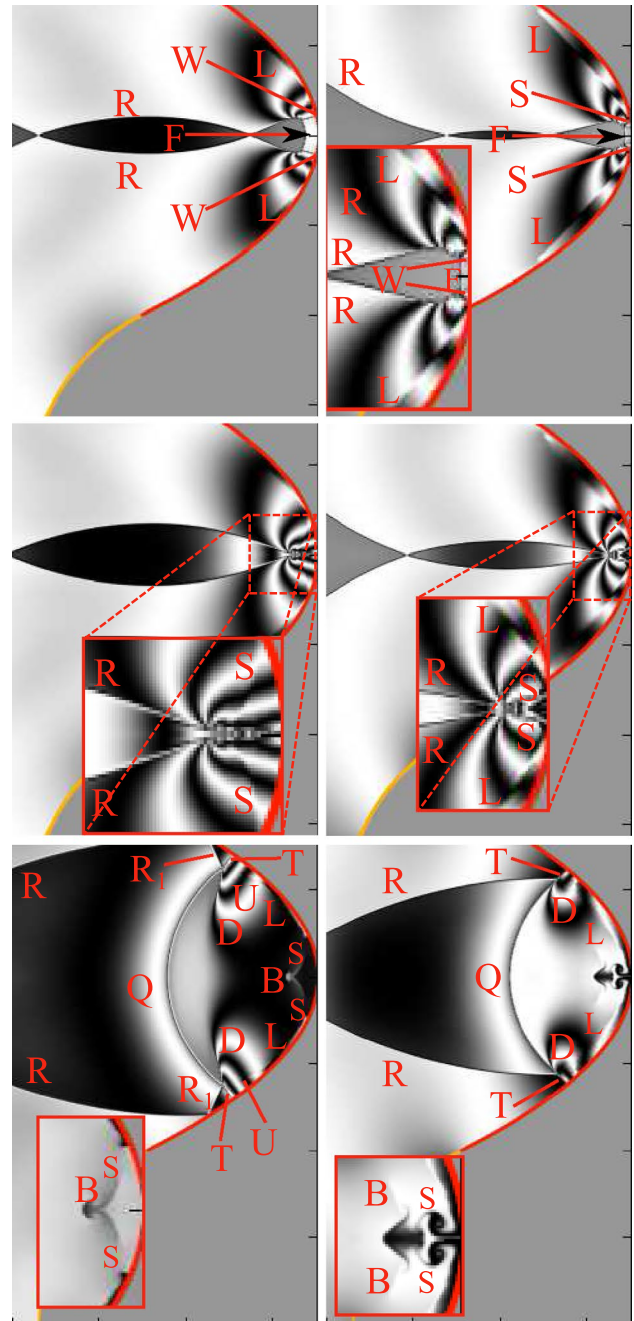

Fig. 45 Numerical interferograms illustrating the pre-focus (first row), focus (second row) and post-focus (third row) shock wave arrangements at M = 1.2 (left column) and 1.45 (right column) for depth-to-aperture ratio of 0.4

Interestingly, the post-focus images for Mach 1.2 show that a regular reflection of the reflected shock wave, R, occurs. The intersection of the reflected shock wave R1 with Mach stem T produces a shear layer, U. In the Mach 1.2 case, the intersection of R1 occurs at the triple point of the Mach reflection formed from the shock waves Q, Mach stem T, and the reflected shock wave D.
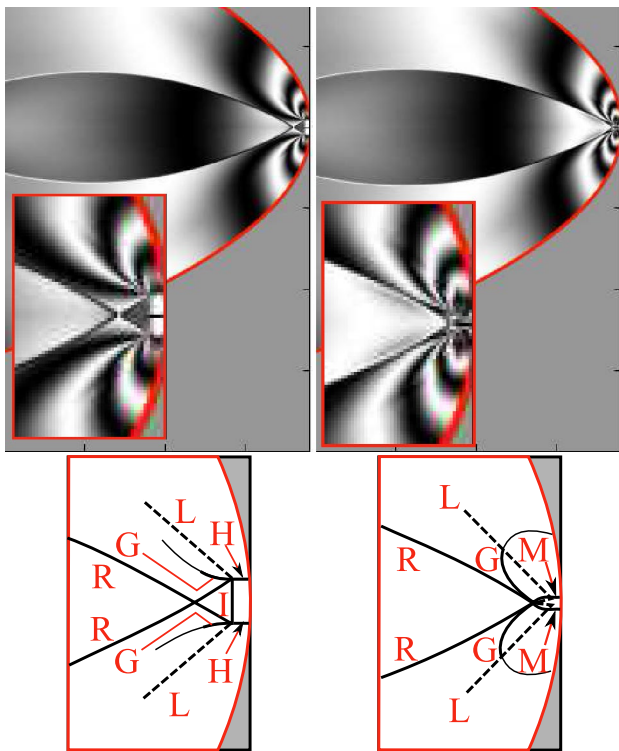
Fig. 46 Numerical interferograms illustrating the pre-focus (left image) and gas dynamic focus (right image) shock wave arrangements at Mach 1.45 with depth-to-aperture ratio of 0.6
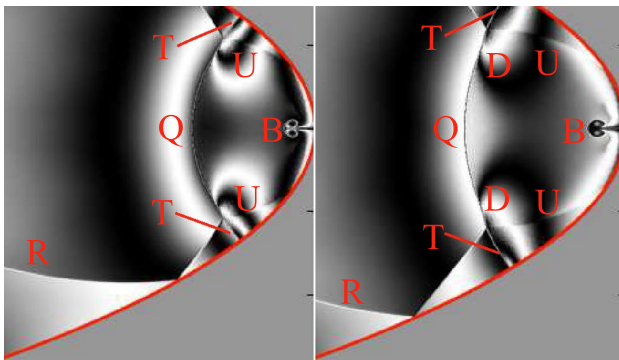

Fig. 47 Post-focus wave configuration visualized using numerical interferometry for the interaction of a Mach 1.45 shock wave with depth-to-aperture ratio of 0.6

The final compound profile investigated, for a depth-to-aperture ratio of 0.6, has a similar initial engagement as for the 0.4 case. Due to the small area in which focus occurs, the numerical interferograms do not provide a clear indication of the exact nature of the focus. Wave diagrams below each image in Fig. 46 provide an interpretation of features. The first frame shows the pre-focus configuration where strong compressions develop adjacent to the Mach stem, H (forming shock wave G), and the incident shock wave, I, is yet to

be reflected from the base of the profile. Then the incident shock wave is fully reflected, most likely forming a Mach reflection consisting of: shock waves, G, a short wall shock, W, and the full reflection of the incident shock wave, I. The main reflected shock wave, M, has formed and the shock system is at focus. Thereafter, the main reflected shock wave expands and the reflected shock waves, G, weaken into compressions preceding the main reflected shock wave.

The post-focus images in Fig. 47 show the development of shear layers along the centre line that have formed two opposite rotating vortices. Mach reflections must have formed earlier producing a short shear layer with a forked pattern similar to other deep cavities. Interestingly, a regular reflection of the reflected shock wave, R, occurs where the reflected shock wave of the regular reflection intersects the Mach stem, T, producing a shear layer, U.

Maps of maximum pressure amplification history for the three compound profiles tested are given in Fig. 48. Increasing maximum pressure occurs with increasing depth, as found for other profiles. However, very similar maximum pressure amplifications, of about 13, are obtained at Mach 1.45 for parabolic and weighted catenary profiles for a depth-to-aperture ratio of 0.75, whereas this value is obtained for the compound profile at a depth-to-aperture ratio of 0.6. Clearly, the inlet has strengthened the shock waves involved in focus, thereby increasing the maximum recorded pressure amplification. Peak pressure amplifications occur in a small area near the base of the profile. The focal areas for the deeper profiles are barely visible due to their proximity to the base of the profile.

7 Conclusion

In general, increases in the depth-to-aperture ratio, for the same reflector profile shape, increased peak pressure amplifications and confirm the results of Nishida (1989). Similarly, increases in incident shock wave strength, for the same reflector profile shape, also serve to increase peak pressure amplifications. In addition, maps of maximum pressure amplifications indicate that increases in the depth-to-aperture ratio, for both standard and compound profiles, reduce focus peak pressure amplifications to an increasingly smaller area that approaches the base of the profile. A combination of the strengthening of the individual shock waves involved in focus, due to profile shape especially if there is an inlet, and the duration of the focus (driven by the reflector shape and incident Mach number) is the primary factors which influence the peak pressure amplifications.

As discussed in Skews and Kleine (2009), it is correct that the shape of perturbations at focus will affect the peak pressure amplifications where nonlinearity tends to spread these perturbations. However, increases in incident shock

Fig. 48 Maps of maximum pressure amplification history for the compound models with depth-to-aperture ratios of 0.2, 0.4 and 0.6 for a Mach 1.45 incident shock
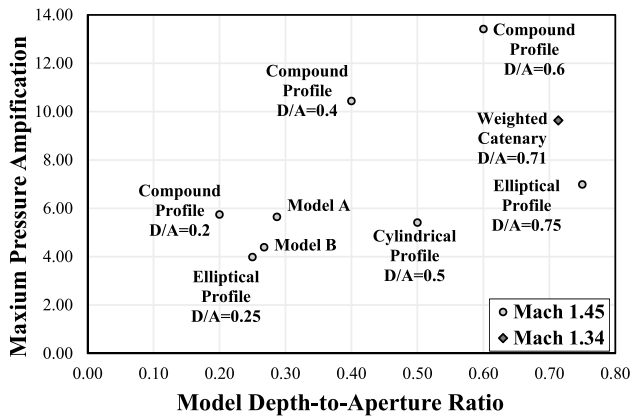

Fig. 49 Maps of maximum pressure amplification history for the compound models with depth-to-aperture ratios of 0.2, 0.4 and 0.6 for a Mach 1.45 incident shock
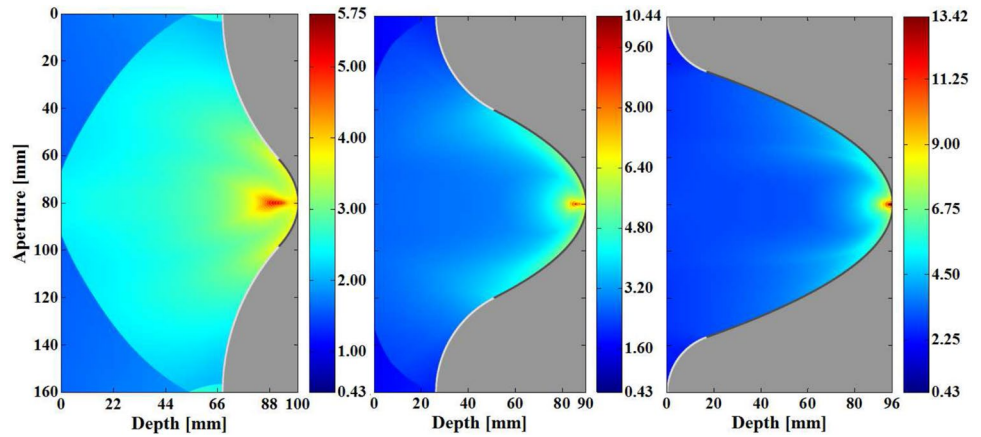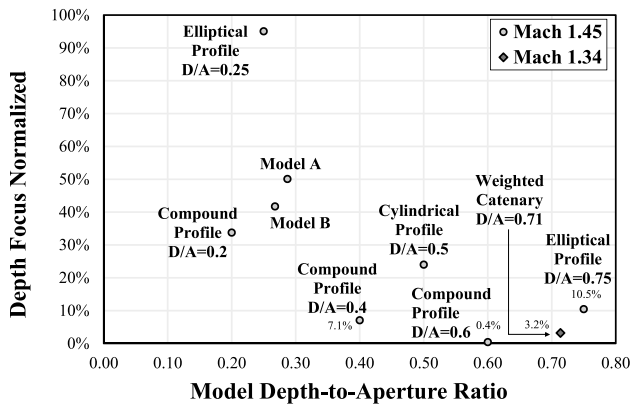

Fig. 50 Peak pressure position normalized to cavity depth

pressure amplification needs to be discussed with respect to the three primary factors indicated in the results above: incident shock wave strength, depth-to-aperture ratio of the profile and, if present, the presence of an inlet. The profile shape, aside from the presence of the inlet, can be regarded as a secondary effect. The results confirm that an inlet can be used to reach higher-pressure amplifications, at lower depth-to-aperture ratios and incident shock wave strengths where the inlet has a significant effect on the shape of the focus region.

These effects, for the non-standard cavities examined, are summarized in Fig. 49.

A similar focusing performance map can be established for the location of the pressure maximum. For the profiles investigated here, this is shown in Fig. 50. Similar to the achievable pressure amplification, the focal area location, expressed as the distance from the base of the reflector normalized by the reflector depth, is a function of reflector shape (including the effect of inlets) and incident shock Mach number. An increase in D/A shifts the focal area closer to the base. Compare, for example, the case of a parabolic cavity with D/A = 0.5 (second row in Fig. 5) with the flow patterns seen for the same shock Mach number in a parabolic cavity of D/A = 1 (Fig. 18). For compound profiles, the trend is amplified, meaning that the addition of an inlet contour further moves the focal area towards the base.

Future work would involve the study of axisymmetric cases and an extension of the current work with more complete performance maps. Experimentally, the measurement of temperature and pressure at the focal region remains a challenge because of the strong temporal and spatial variations.

strength for a fixed-focus topology appear to increase the maximum recorded pressure amplification. Therefore, peak

References

Apazidis N, Eliasson V (2019) Shock focusing phenomena. Springer, Berlin

Apazidis N, Kjellander M, Tillmark N (2012) High Energy concentration by symmetric shock focusing. In: Kontis K (ed) 28th International symposium on shock waves. Springer, Berlin

Babinsky H, Onodera O, Takayama K, Saito T, Voinovich P, Timofeev E (1998) The influence of entrance geometry of circular reflectors on shock wave focusing. Comput Fluids 27:611–618

Barth TJ, Jesperson DC (1989) The design and application of upwind schemes on unstructured meshes. AIAA paper. 89–0366

Ben-Dor G (2007) Shock wave reflection phenomena, 2nd edn. Springer, Berlin

Ben-Dor G, Takayama K (1986–87) The dynamics of the transition from Mach to regular reflection over concave cylinders. Israel J Tech 23:71–74

Bond C, Hill DJ, Meiron DI, Dimotakis PE (2009) Shock focusing in a planar convergent geometry: experiment and simulation. J Fluid Mech 641:297–333

Cates J, Sturtevant B (1987) Shock wave focusing using geometrical shock dynamics. Phys Fluids 9(30):3068

Dennen RS, Wilson LN (1962) Electrical generation of imploding shock waves. In: Chace WG, Moore HK (eds) Exploding wires. Plenum Press, New York, pp 145–157

Grönig H (1986) Shock wave focusing phenomena. In: Shock waves and shock tubes, 15th International symposium, Berkeley. Stanford University Press, pp 43–56

Gruber S, Skews B (2013) Weak shock wave reflection from concave surfaces. Exp Fluids 54:1571

Guderley G (1941) Starke kugelige und zylindrische Verdichtungsstöße in der Nähe des Kugelmittelpunktes bzw. der Zylinderachse. Luftfahrtforsch 29(9):302–312

Gustafsson G (1987) Experiments on shock-wave focusing in an elliptical cavity. J Appl Phys 61:5193–5195

Inoue O, Imuta G, Milton BE, Takayama K (1995) Computational study of shock wave focusing in a log-spiral duct. Shock Waves 5:183–188

Izumi K, Aso S, Nishida M (1994) Experimental and computational studies focusing processes of shock waves reflected from parabolic reflectors. Shock Waves 3:213–222

Kim H-D, Kweon Y-H, Setoguchi T, Matsuo S (2003) A study on the focusing phenomenon of a weak shock wave. Proc Instn Mech Engrs 217:1209–1220

Kleine H (2001) Measurement techniques and diagnostics: flow visualization. In: Ben-Dor G, Igra O, Elperin T (eds) Handbook of shock waves, vol 1. Academic Press, San Diego, pp 685–738

Knystautas R, Lee B, Lee J (1969) Diagnostic experiment on converging detonations. Phys Fluids Suppl 1:165–168

Liang SM, Wu LN, Hsu RL (1999) Numerical investigation of axisymmetric shock wave focus over paraboloidal reflectors. Shock Waves 9:367–379

Liou M-S (1996) A sequel to AUSM: AUSM+. J Comput Phys 129:36–382

MacLucas DA (2012) Shock wave-induced flow features in concave profiles. Doctoral thesis, University of the Witwatersrand, South Africa

MacLucas DA, Skews BW, Kleine H (2015) High-speed imaging of shock wave focusing in concave profiles using shearing interferometry and direction-indicating colour schlieren. J Vis 18:521–529

Marchiano R, Coulouvrat F, Grenon R (2003) Numerical simulation of shock wave focusing at fold caustics, with application to sonic boom. J Acoust Soc Am 114(4):1758–1771

Nishida M (1989) Focusing of reflected shock waves. In: Proceedings of the international workshop on shock wave focusing, ed. Takayama, K. Shock Wave Research Center, Institute of Fluid Science, Tohoku University, Sendai, Japan, pp 141–153

Oertel H, Oertel H (1989) Optische Strömungsmeßtechnik. Karlsruhe, G. Braun

Perry RW, Kantrowitz A (1951) The production and stability of converging shock waves. J Appl Phys 22:878–886

Shadloo MS, Hadjadj A, Chaudhuri A (2014) On the onset of postshock flow instabilities over concave surfaces. Phys Fluids 26(7):076101

Skews BW, Kleine H (2009) Shock wave interactions with concave cavities. In: Hannemann K, Seiler F (eds) 26th International symposium of shock waves. Springer, pp 1485–1490

Skews BW, Kleine H, Barber T, Iannucelli M (2007) New flow features in a cavity during shock wave impact. 16th Australasian fluid mechanics conference, Gold Coast, Australia

Skews BW, Kleine H (2007) Flow features resulting from shock wave impact on a cylindrical cavity. J Fluid Mech 580:481–493

Skews BW, Kleine H (2009) Unsteady flow diagnostics using weak perturbations. Exp Fluids 46:65–76

Sturtevant B (1989) The physics of shock focusing in the context of ESWL. In: Proceedings of the international workshop on shock wave focusing, ed. Takayama, K. Shock Wave Research Center, Institute of Fluid Science, Tohoku University, Sendai, Japan, pp 39–64. Sendai

Sturtevant B, Kulkarny VA (1976) The focusing of weak shock waves. J Fluid Mech 76:651–671

Taieb D, Ribert G, Hadjadj A (2010) Numerical simulations of shock focusing over concave surfaces. AIAA J 48(8):1739–1747

Takayama K (2019) Visualization of shock wave phenomena. Springer, Berlin. https://doi.org/10.1007/978-3-030-19451-2

Springer